IMA Journal of Applied Mathematics (2015) **80**, 1582–1618
doi:10.1093/imamat/hxv009
Advance Access publication on 9 May 2015

Incipient mixing by Marangoni effects in slow viscous flow of two immiscible fluid layers

LYDIA M. RICKETT
School of Mathematics, University of East Anglia, Norwich NR4 7TJ, UK and The Sainsbury Laboratory, Norwich Research Park, Norwich NR4 7UH, UK
lydia.rickett@sainsbury-laboratory.ac.uk

ROBERT PENFOLD*
Institute of Food Research, Norwich Research Park, Norwich NR4 7UA, UK
*Corresponding author: robert.penfold@ifr.ac.uk

AND

MARK G. BLYTH, RICHARD PURVIS AND MARK J. COOKER
School of Mathematics, University of East Anglia, Norwich NR4 7TJ, UK

[Received on 28 October 2014; revised on 18 March 2015; accepted on 8 April 2015]

Ignoring inertia, a deformable interface separating two fluid films is considered, subject to non-uniform tension driven by the solutal Marangoni effect in the presence of a scalar concentration field. Detailed description of adsorption kinetics is abrogated by a simple ansatz directly relating interfacial tension and bulk solute concentration. Consequently, the formal mathematical treatment and some of the results share features in common with the Rayleigh–Bénard–Marangoni thermocapillary problem. Normal mode perturbation analysis in the limit of small interface deformations establishes the existence of an unstable response for low wavenumber excitation. In the classification of Cross & Hohenberg (1993, Pattern formation outside of equilibrium. *Rev. Mod. Phys.*, **65**, 851–1112), both type I and type II behaviour are observed. By considering the zero wavenumber situation exactly, it is proved that all eigenvalues are purely imaginary with non-positive imaginary part; hence, a type III instability is not possible. For characteristic timescales of mass diffusion much shorter than the relaxation time of interfacial fluctuations (infinite crispation number): the response growth rate is obtained explicitly; only a single excitation mode is available, and a complete stability diagram is constructed in terms of the relevant control parameters. Otherwise, from a quiescent base state, an infinite discrete spectrum of modes is observed that exhibit avoided crossing and switching phenomena, as well as exceptional points where stationary state pairs coalesce into a single oscillatory standing wave pattern. A base state plane Poiseuille flow, driven by an external pressure gradient, generally exaggerates the response: growth rates of instabilities are enhanced, and stable decay is further suppressed with increasing base flow speed, but the inherent symmetry breaking destroys stationary and standing wave response. Results are obtained in this most general situation by implementing a numerical Chebyshev collocation scheme. The model was motivated by hydrodynamic processes supposed to be involved in gastric digestion of humans.

Keywords: liquid–liquid interface; Gibbs elasticity; Stokes flow; linear stability analysis; generalized eigenvalue problem; collocation method; avoided crossing; exceptional point.

1. Introduction

To understand the bioavailability and delivery of nutrients and medicines from processed foods and pharmaceutical preparations, a detailed mechanistic model of digestion is needed. The human gastrointestinal tract, from the mouth to the anus, is a coupled sequence of specialized organs, each of which has a distinctive digestive function. In particular, the stomach performs biochemical tasks involving complex salts, strong mineral acid and proteolytic enzymes to produce chyme (soft solid, partially digested food; Kong & Singh 2008). The stomach also offers a prominent line of defence against pathogenic microorganisms, but more importantly, it is the primary site of mechanical action where ingested material is subjected to a complicated unsteady shear flow, dominated by frictional dissipation rates with relatively negligible inertial forces (Pal *et al.*, 2007). For the purpose of developing a simple mathematical model of this action, we shall adopt here the following working definition: 'digestion' means the incipient mixing associated with the linear temporal instability of the interface between two immiscible liquids. Agitated away from equilibrium, the morphological evolution of interfacial patterns and the dynamics of viscous interfacial flow are driven by the physical mechanisms of heterogeneous mixing (Pozrikidis, 1997). Despite the absence of inertia-driven turbulence, a combination of chaotic advection and diffusion can promote mixing in Stokes flows (Thiffeault *et al.*, 2011) that are governed by time-reversible equations of motion. With deformable boundaries, a 'geometric' mixing mechanism has also been suggested exploiting anholonomy of the system, so that flow variables do not recover their original values on negotiating a closed loop in the parameter space (Cartwright *et al.*, 2012).

Developed at the Institute of Food Research (UK), the dynamic gastric model (DGM) is an *in vitro* system that automatically simulates human digestion for the first time from a realistic physiological perspective by accounting for the physical, mechanical and biochemical environment experienced in the stomach (Mercuri *et al.*, 2011; Chessa *et al.*, 2014). To establish a reliable predictive relationship between DGM output and physiological stomach behaviour, some quantitative analysis of the device function is required. Motivated by this need, the present work establishes conditions relevant to the hydrodynamics of digestion insofar as they may lead to mixing and may be a precursor for turbulence.

The application of Orr–Sommerfeld perturbation analysis (Drazin, 2002; Charru, 2011) for parallel fluid flows has a rich, mature and growing literature. Linear response theory leads to a generalized eigenvalue problem, which has a non-trivial solution only if the temporal and spatial frequencies are linked by a dispersion relation. In the most general problem, the large number of control parameters (at least six) spawns a host of potentially unstable modes governed by diverse mechanisms of different physical origin. The viscosity-induced interfacial mode instability of two superposed and bounded fluid layers was first discussed by Yih (1967). Subsequently designated as 'the thin-layer effect' (Hooper, 1985), a spatially confined film of more viscous fluid is unstable to long waves at all positive Reynolds numbers. For the converse situation of a confined film of lower viscosity, the flow is stable in the limit of weak interfacial tension (Renardy, 1987a). The thin-layer effect is also observed for multiple fluid layer configurations in plane Poiseuille flow (Anturkar *et al.*, 1990). Neglecting interfacial tension entirely, Charru & Hinch (2000) have neatly rationalized Yih's small wavenumber analysis together with a second instability at low Reynolds number and high frequency (Hooper & Boyd, 1983) that is present between two shearing unbounded fluids. This latter phenomenon has been confirmed by numerical volume-of-fluid studies in the non-linear regime (Coward *et al.*, 1997; Li & Renardy, 2000) and might be regarded as a viscous analogue of the Kelvin–Helmholtz instability. Hinch (1984) proposed a detailed mechanism and concluded that some small inertial contribution is necessary in order that advection by the main shear flow can drive the disturbance vorticities in each fluid out-of-phase and so allow the induced velocity fields to amplify the interfacial perturbation. By considering the energy budget in low

Reynolds number expansions, Albert & Charru (2000) have confirmed that interfacial instability arises from inertia influencing disturbances, at both small and large wavenumber.

It is perhaps because of this conclusion that the stability of superposed liquid layers in strict Stokes flow (at zero Reynolds number) has received far less attention. Pozrikidis (1997) has implemented a boundary integral method to investigate the interfacial behaviour subject to *finite* amplitude perturbations. He showed that sufficiently large amplitude disturbances cause permanent interfacial deformation with a morphology that depends sensitively on the viscosity ratio. In a very recent study of Poiseuille flow of layered *miscible* fluids in the Stokes regime, Talon & Meiburg (2011) have reported that diffusion has a destabilising effect very similar to that induced by inertia at finite Reynolds number. Instead of a macroscopically sharp discontinuity in fluid properties, partial bulk miscibility influences stability by smearing the interface over a finite width (Anderson *et al.*, 1998). This diffuse and inhomogeneous transition zone is typically modelled (Sahu *et al.*, 2009a,b) by a smooth viscosity distribution coupled to a convective–diffusion equation for a scalar concentration field of 'friction-inducing solute'. Formally, this is very similar to our present treatment of Marangoni effects (Johnson & Narayanan, 1997) where spatial variations of interfacial tension are produced, for example, by a temperature field or by a non-uniform distribution of surfactants. This artifice will simplify the differential geometry and obviate a detailed chemical kinetic mechanism of the interfacial adsorption process (Palmer & Berg, 1972; Reichenbach & Linde, 1981; Slavtchev *et al.*, 1998, 2006) that is highly complicated in typical applications, notably the digestion mechanism of the stomach.

Another consequence is the manifestation of a formal correspondence between this approach and the analysis of thermal Marangoni effects (Nepomnyashchy *et al.*, 2006). As a rich example of spontaneous pattern formation in non-equilibrium dynamical systems, the classical Rayleigh–Bénard convective instability (Koschmieder, 1974) of a single fluid layer subjected to a transverse temperature gradient has been long studied (Normand *et al.*, 1977) but continues to attract attention (Bodenschatz *et al.*, 2000). For a stratified superposition of several immiscible fluids, many new and qualitatively different phenomena arise from the competition of individual layer instabilities (Andereck *et al.*, 1998). By assuming 'exchange of stabilities' (Drazin & Reid, 2004), a linear stability analysis of the thermal Marangoni effect was tackled by Zeren & Reynolds (1972), and subsequently extended by Zhao *et al.* (1995) to account for interfacial deformation. Rasenat *et al.* (1989) completed a more general treatment to demonstrate that steady convection could be driven either by buoyancy or by Marangoni forces. For thin film flows, the mathematical analysis exploits disparity in length scales to simplify the field equations, but microscopic surface forces of van der Waals or electromagnetic origin can also become asymptotically important (Oron *et al.*, 1997; Craster & Matar, 2009). The non-linear evolution of interfacial deformation arising from a small wavenumber perturbation (the 'long-wave' limit) is governed by a Cahn–Hilliard equation that describes the ('phase') transition between monotonic and stationary instabilities, in analogy with thermodynamic spinodal decomposition (Merkt *et al.*, 2005; Nepomnyashchy *et al.*, 2006).

Frenkel & Halpern (2002) and Halpern & Frenkel (2003) have identified a new non-inertial interfacial instability, which was investigated further by Blyth & Pozrikidis (2004a). This is driven by the Marangoni traction that arises from the presence of adsorbed surfactant and velocity shear in two-layer planar flows of Couette–Poiseuille type. A physical mechanism is also proposed where the imbalance of interfacial tension drives flow from troughs to peaks and reinforces the deformation. Notably, in contrast to the interfacial mode of inertial flows, a viscosity jump is not required for instability. Moreover, explicit analytic expressions are obtained for the wave speed and growth rate. Corresponding phenomena are also predicted for surfactant-laden interfaces in gravity-driven flow on an inclined plane (Blyth & Pozrikidis, 2004b; Gao & Lu, 2007) and for radially stratified films in concentric two-fluid Taylor–Couette flow (Peng & Zhu, 2010), where there is a complicated interaction of instability mechanisms. The effect of inertia coupled with the Marangoni instability has also been studied by normal-mode analysis (Blyth & Pozrikidis, 2004c; Frenkel & Halpern, 2005) and numerical methods (Pozrikidis, 2004) applicable beyond the linear regime. A wider range of unstable wavenumbers is the chief consequence. Noting that insoluble surfactant cannot destabilize a sheared interface between two semi-infinite fluids, Pozrikidis & Hill (2011) have recently questioned the necessity of a bounded fluid domain to realize the Marangoni instability. They concluded that one wall is required to engage the Marangoni mechanism, but the presence of a second wall may stabilise the flow.

Section 2 sets out the physical arguments to establish the appropriate governing equations and boundary conditions. A full mathematical treatment is developed in Section 3, culminating in a dispersion relation. Two special cases are considered in Section 4 before the general solution is presented in Section 5. Results are collected and discussed in Section 6, and the paper concludes in Section 7 with some perspective on applications and future work. Appendix A contains comprehensive mathematical details and formal proofs of some results in the text.

2. Mathematical model specification

2.1 *Physical situation: the dynamic gastric model*

With its modular design, the DGM separates two primary anatomical features of the human stomach: the proximal cardia/fundus/main body that receives material from the oesophagus, and the distal pyloric antrum where chyme is produced before discharge to the duodenum (Wickham *et al.*, 2012). The pseudo-main body comprises a thermally jacketed elastic cone, hydraulically driven by cyclic pumping to generate a specific inhomogeneous mixing behaviour and hydration patterns that closely resemble observations *in vivo* (Marciani *et al.*, 2001, 2006, 2009). A computer-controlled feedback loop monitors temperature and pH in real time to govern the injection of surfactants, acids/bases and proteolytic solutions that correspond to gastric secretions. An intervening valve regulates residence times before partial emptying into a pseudo-antrum where digesta are subjected to periodic high shear fields that force mechanical breakdown of the food structure.

In operation (Wickham *et al.*, 2012), aqueous gastric solution enters the DGM fundus under gravity from an annular distributor, suspended coaxially above the main body, and flows in a thin film down the interior surface of the conical vessel (Fig. 1). The main body is then charged with ‘ingested’ material, typically a heterogeneous viscoelastic food product, but most simply with a Newtonian liquid. Gentle deformations of the elastic main body wall are actuated by driven pressure variation of the external thermal bath. The observed digestion process has the character of ‘onion peeling’ where thin layers of ingested material are progressively sloughed off to enter the lower antral chamber. The DGM main body has geometric and material features in common with the intensively studied core-annular pipe flow (Renardy, 1987b; Joseph *et al.*, 1997) used for the efficient water lubricated transport of heavy crude oils, emulsions or bitumen froths, but differs in the steeply converging tube arrangement with weakly deformable walls and a much lower flow rate.

To simplify the problem, a general non-Newtonian food material of spatially inhomogeneous transport properties is idealized as a discrete ternary mixture of uniform macroscopic phases. Further, the main food bolus is regarded as effectively solid and suspended at neutral buoyancy in the main body device. We assume that the ‘onion-peeling’ process is confined to a relatively thin sleeve of liquid material that separates the bolus from the main body wall where most gastric chemistry takes place. This sleeve is treated as a uniform slab confining two immiscible liquids that are possibly subject to a

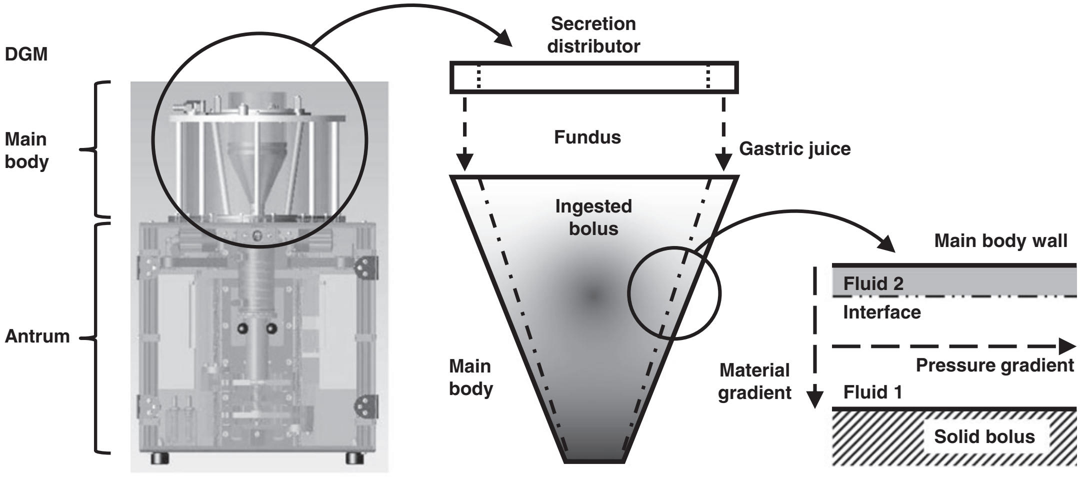

FIG. 1. Cartoon illustrates the modelling abstraction from the physical DGM device to the mathematical idealization.

constant longitudinal pressure gradient. Finally, a scalar material field is imposed that interacts with the tension of the interface to represent the biological activity of gastric secretions including acids, enzymes and surfactants. The solid food bolus and the main body wall are supposed porous to the solute material. Although the DGM main body wall is actually impermeable, this last assumption is more realistic in terms of the physiological organ and symmetrises the solute boundary conditions in our analysis. These modelling abstractions are illustrated by the cartoon in Fig. 1.

2.2 *Coordinate frame, constitutive relation and non-dimensionalization*

Under isothermal conditions, consider the unidirectional creeping flow of two incompressible Newtonian fluids (indexed by the labels $j = 1, 2$), driven by a constant axial pressure gradient $-\tilde{G}_{\rm p}$ (with $\tilde{G}_{\rm p} \geqslant 0$) through an infinite channel bounded by stationary parallel walls fixed at separation $2\tilde{h}$ (see Fig. 2). It is natural to adopt a Cartesian system $(\tilde{x},\ \tilde{y},\ \tilde{z})$ with the longitudinal coordinate $-\infty < \tilde{x} < \infty$ and the transverse coordinate $-\tilde{h} \leqslant \tilde{y} \leqslant \tilde{h}$. Unit vectors in each coordinate direction are denoted $\mathbf{i}$, $\mathbf{j}$ and $\mathbf{k}$, respectively. Interfacial disturbances are supposed small and are manifest in two spatial dimensions only, so that all the relevant dynamical quantities are independent of the lateral coordinate $\tilde{z}$. The fluid labelled 1 is confined between the lower wall at $\tilde{y} = -\tilde{h}$ and the interface, whose flat equilibrium position is $\tilde{y} = \tilde{\alpha}$, where $\tilde{\alpha}$ is a constant (see Fig. 2). Each of the bulk fluids is characterized by a dynamic viscosity $\tilde{\mu}_j$ and a diffusion coefficient $\tilde{D}_j$ for solute species. We observe the Boussinesq approximation and suppose that all $\tilde{\mu}_j$ and $\tilde{D}_j$ are constant and remain unaffected by variations in bulk solute concentration. Furthermore, there is no stratification in mass density $\tilde{\rho}_1 = \tilde{\rho}_2 = \tilde{\rho}$, and the system is assumed free of external body forces, so buoyancy effects are neglected.

The deformable interface located at $\tilde{y} = \tilde{\eta}(\tilde{x},\ \tilde{t})$ is a free material boundary with a Newtonian response: explicit effects of interfacial rheology are neglected. Nevertheless, the associated equilibrium interfacial tension is a sensitive function of the local environment, with a complicated dependence on temperature and the presence of solutes in either of the adjoining fluid phases. Spatial inhomogeneities of the interfacial tension can arise from fluctuations in the physical adsorption of surfactants

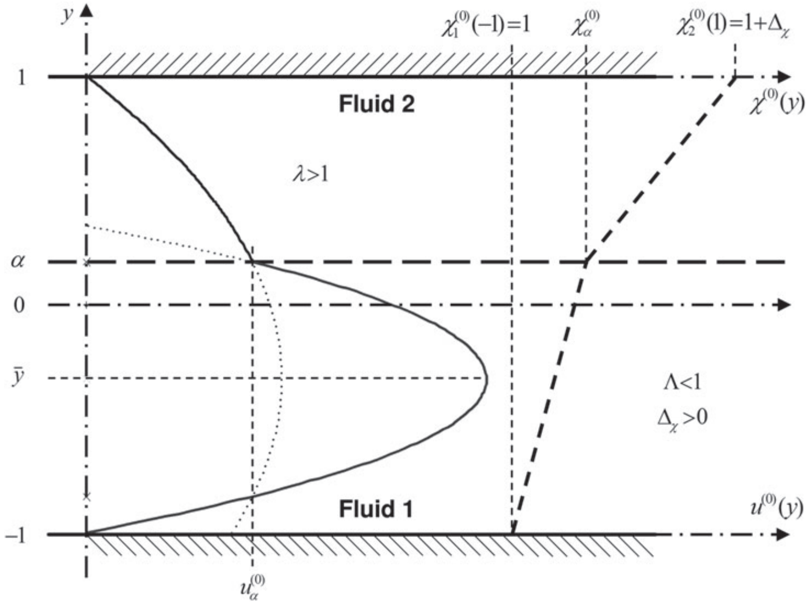

FIG. 2. The basic states of fluid flow and concentration distribution are shown with the geometry and coordinate variables defined in the text.

and advective interfacial transport, or from localized chemical activity at the interface. For simplicity, we posit a scalar field $\tilde{\chi}_j = \tilde{\chi}_j(\tilde{x}, \tilde{y}, \tilde{t})$ to represent the concentration of some surface active species dissolved in fluid j, that is subject to advection and diffusion in the three-dimensional bulk phases only. It is here that our ansatz deviates from other studies of the solutal Marangoni effect (Li & Pozrikidis, 1997; Frenkel & Halpern, 2002; Halpern & Frenkel, 2003; Blyth & Pozrikidis, 2004a,c; Pozrikidis, 2004; Frenkel & Halpern, 2005; Gao & Lu, 2007; Pozrikidis & Hill, 2011) where the surfactant is assumed insoluble in bulk, confined strictly to the interface and governed by an appropriate two-dimensional transport equation. In accord with our DGM idealization, Dirichlet conditions are prescribed on $\tilde{\chi}_j$ at the bounding walls which, although stationary, support a diffusive flux of solute material to adjacent 'notional' phases. Thus, under the influence of a concentration gradient, the solute is allowed to spread by Brownian motion but without advection into the food bolus and the gastric mucosa that confine the fluid slab: the static walls are porous to solute but impermeable to solvent.

We undertake a temporal linear stability analysis of steady base state flow with a uniform interfacial tension and concentration fields

$$\tilde{\chi}_j^{(0)} = \tilde{\chi}_j^{(0)}(\tilde{y}), \quad j \in \{1,\ 2\}, \tag{2.1}$$

that depend only on the transverse coordinate across the channel. For small perturbations of the base state flow, the change in the interfacial tension is proportional to the induced departure of the bulk concentration from $\tilde{\chi}_j^{(0)}$, and proportional to a contribution that arises from displacement of the interface within the static field. We adopt the linear interfacial equation of state

$$\tilde{\gamma} = \tilde{\gamma}(\tilde{x}, \tilde{y}, \tilde{t}) = \tilde{\gamma}_0 \left(1 - \mathrm{Mg} \times \left(\frac{\tilde{\chi}_j(\tilde{x}, \tilde{y}, \tilde{t}) - \tilde{\chi}_j^{(0)}(\tilde{\alpha})}{\tilde{\chi}_2^{(0)}(\tilde{h}) - \tilde{\chi}_1^{(0)}(-\tilde{h})}\right)\right), \tag{2.2}$$

TABLE 1 *The seven dimensionless control parameters that feature in this analysis*

Mg	=	$\dfrac{\tilde{\chi}_2^{(0)}(\tilde{h})-\tilde{\chi}_1^{(0)}(-\tilde{h})}{\tilde{\gamma}_0}\left(\dfrac{\partial\tilde{\gamma}}{\partial\tilde{\chi}_j}\right)$	Dilatational elasticity of interface
Cr	=	$\dfrac{\tilde{\mu}_1\tilde{D}_1}{\tilde{h}\tilde{\gamma}_0}$	Crispation number
Eu	=	$\dfrac{\tilde{h}^2\tilde{G}_\mathrm{p}}{\tilde{\gamma}_0}$	Euler number
$\varDelta_\chi$	=	$\dfrac{\tilde{h}\tilde{\gamma}_0}{\tilde{\mu}_1^2}(\tilde{\chi}_2^{(0)}(\tilde{h})-\tilde{\chi}_1^{(0)}(-\tilde{h}))$	Overall solute concentration difference
λ	=	$\dfrac{\tilde{\mu}_2}{\tilde{\mu}_1}$	Dynamic viscosity ratio
$\varLambda$	=	$\dfrac{\tilde{D}_2}{\tilde{D}_1}$	Solute diffusivity ratio
δ	=	$\dfrac{1-\tilde{\alpha}/\tilde{h}}{1+\tilde{\alpha}/\tilde{h}}$	Fluid film thickness ratio

with the understanding that physical meaning is attached to this field $\tilde{\gamma}$ only for $\tilde{y}=\tilde{\eta}$. The dimensionless interaction parameter Mg measures the change in interfacial tension with respect to the local concentration of surface active solutes and is related to the dilatational (Gibbs) elasticity that couples the dynamic boundary conditions on interfacial stress and surfactant flux (Edwards *et al.*, 1991). Typically, $\mathrm{Mg}>0$ and the spontaneous physical adsorption of material at the interface will lower the surface free energy relative to the bulk phases. We are also interested, however, in the more complex situation where changes of interfacial tension are driven by chemical activity. For example, denaturation, cross-linking or gelation of proteins at the interface may lead to *increases* of tension compared with the bare surface. Within the ansatz (2.2), this behaviour could be modelled by choosing $\mathrm{Mg}<0$, that is the solutal analogue of the anomalous thermocapillary effect (Braverman *et al.*, 2000).

To accommodate the analysis of a quiescent base state with a vanishing pressure gradient $\tilde{G}_\mathrm{p}=0$, suitable units of mass, length and time are, respectively,

$$[\tilde{M}]=\frac{(\tilde{h}\tilde{\mu}_1)^2}{\tilde{\gamma}_0},\quad [\tilde{L}]=\tilde{h},\quad [\tilde{T}]=\frac{\tilde{h}\tilde{\mu}_1}{\tilde{\gamma}_0}. \tag{2.3}$$

Accordingly, the dynamics depends on at most seven dimensionless control parameters listed in Table 1. From now on, all dimensionless quantities will be indicated by the absence of tilde decoration.

2.3 *Governing equations*

In the effective two-dimensional geometry, we have the Stokes stream functions $\psi_j=\psi_j(x,y,t)$ satisfying biharmonic equations

$$\nabla^4\psi_j=\left(\frac{\partial^4}{\partial x^4}+2\frac{\partial^4}{\partial x^2\partial y^2}+\frac{\partial^4}{\partial y^4}\right)\psi_j=0, \tag{2.4}$$

that determine the velocity fields $\mathbf{u}_j = u_j\mathbf{i} + v_j\mathbf{j}$ with longitudinal and transverse components

$$u_j = \frac{\partial \psi_j}{\partial y} \quad \text{and} \quad v_j = -\frac{\partial \psi_j}{\partial x}. \tag{2.5}$$

Incorporating the pressure fields $p_j = p_j(x, y, t)$, the Newtonian stress tensors are

$$\boldsymbol{\sigma}_j = \boldsymbol{\sigma}_j(x, y, t) = -p_j\mathbf{I} + \lambda_j(\nabla\mathbf{u}_j + (\nabla\mathbf{u}_j)^\top), \tag{2.6}$$

where $\lambda_1 = 1$ and $\lambda_2 = \lambda$. The concentration fields are subject to fluid advection and bulk diffusion, described as

$$\left(\frac{\partial}{\partial t} + \mathbf{u}_j \cdot \nabla - \mathrm{Cr}\,\Lambda_j\nabla^2\right)\chi_j = 0, \tag{2.7}$$

where $\Lambda_1 = 1$ and $\Lambda_2 = \Lambda$.

With the interface position at $y = \eta(x, t)$, the field equations (2.4) and (2.7) are supplemented by no-slip and kinematic boundary conditions:

$$\begin{array}{ll}
u_1(x, -1, t) = 0, \quad u_2(x, 1, t) = 0, & \text{(no slip on walls)} \\
v_1(x, -1, t) = 0, \quad v_2(x, 1, t) = 0, & \left(\begin{array}{c}\text{stationary, solvent} \\ \text{impermeable walls}\end{array}\right) \\
\left.\begin{array}{l}(u_1 - u_2)(x, \eta, t) = 0 \\ (v_1 - v_2)(x, \eta, t) = 0\end{array}\right\}, & \left(\begin{array}{c}\text{flow continuity} \\ \text{on interface}\end{array}\right) \\
\dfrac{\partial \eta}{\partial t} + u_j(x, \eta, t)\dfrac{\partial \eta}{\partial x} - v_j(x, \eta, t) = 0. & \left(\begin{array}{c}\text{moving material} \\ \text{interface}\end{array}\right)
\end{array} \tag{2.8}$$

Given local orthogonal unit vectors perpendicular $\hat{\mathbf{n}} = \hat{\mathbf{n}}(x, \eta, t)$ (directed from fluid 2 into fluid 1) and tangent $\hat{\mathbf{t}} = \hat{\mathbf{t}}(x, \eta, t)$ to the interface, the corresponding components of the dynamic stress balances become, respectively,

$$\begin{aligned}
\hat{\mathbf{n}} \cdot ((\boldsymbol{\sigma}_1 - \boldsymbol{\sigma}_2)(x, \eta, t)) \cdot \hat{\mathbf{n}} &= \left(1 + \left(\frac{\partial \eta}{\partial x}\right)^2\right)^{-3/2} \frac{\partial^2 \eta}{\partial x^2}\gamma(x, \eta, t), \\
\hat{\mathbf{t}} \cdot ((\boldsymbol{\sigma}_1 - \boldsymbol{\sigma}_2)(x, \eta, t)) \cdot \hat{\mathbf{n}} &= -\left(1 + \left(\frac{\partial \eta}{\partial x}\right)^2\right)^{-1/2} \left(\frac{\partial \gamma}{\partial x}(x, \eta, t) + \frac{\partial \eta}{\partial x}\frac{\partial \gamma}{\partial y}(x, \eta, t)\right).
\end{aligned} \tag{2.9}$$

Finally, concentrations are prescribed on the walls, together with interfacial continuity conditions on the χ_j and the material flux according to

$$\begin{array}{ll}
\left.\begin{array}{l}\chi_1(x, -1, t) = 1 \\ \chi_2(x, 1, t) = 1 + \Delta_\chi\end{array}\right\}, & \left(\begin{array}{c}\text{prescribed wall} \\ \text{concentration}\end{array}\right) \\
(\chi_1 - \chi_2)(x, \eta, t) = 0, & \left(\begin{array}{c}\text{concentration continuity} \\ \text{on interface}\end{array}\right) \\
\frac{\partial}{\partial y}(\chi_1 - \Lambda\chi_2)(x, \eta, t) = 0. & \left(\begin{array}{c}\text{concentration flux} \\ \text{continuity on interface}\end{array}\right)
\end{array} \tag{2.10}$$

3. General analysis of the mathematical model

3.1 *Base (ground) state: unperturbed flow*

For steady plane Poiseuille flow with a flat interface $\eta(x) = \alpha$, we obtain the pressure fields

$$p_j^{(0)} = p_j^{(0)}(x) = p_0 - \mathrm{Eu}\, x, \tag{3.1}$$

where p_0 is a constant background pressure and Eu is the Euler number (Table 1). Similarly, the velocity fields are (see Fig. 2)

$$\begin{aligned} u_1^{(0)}(y) &= u_\alpha^{(0)} + \frac{\mathrm{Eu}}{2}(\alpha - y)\left(y - \frac{\delta - \lambda}{\delta + \lambda}\right) = \frac{\partial \psi_1^{(0)}}{\partial y}, \quad v_1^{(0)} = 0, \quad (-1 \leqslant y \leqslant \alpha), \\ u_2^{(0)}(y) &= u_\alpha^{(0)} - \frac{\mathrm{Eu}}{2\lambda}(y - \alpha)\left(y - \frac{\delta - \lambda}{\delta + \lambda}\right) = \frac{\partial \psi_2^{(0)}}{\partial y}, \quad v_2^{(0)} = 0, \quad (\alpha \leqslant y \leqslant 1), \end{aligned} \tag{3.2}$$

where the horizontal velocity at the interface is

$$u_\alpha^{(0)} = \frac{2\delta\,\mathrm{Eu}}{(1+\delta)(\delta+\lambda)}. \tag{3.3}$$

The steady concentration fields are (see Fig. 2)

$$\begin{aligned} \chi_1^{(0)}(y) &= \chi_\alpha^{(0)} - G_{\chi,1}(\alpha - y), \quad (-1 \leqslant y \leqslant \alpha), \\ \chi_2^{(0)}(y) &= \chi_\alpha^{(0)} + G_{\chi,2}(y - \alpha), \quad (\alpha \leqslant y \leqslant 1), \end{aligned} \tag{3.4}$$

where the unperturbed interfacial concentration and corresponding gradients are

$$\chi_\alpha^{(0)} = \frac{\delta + \Lambda(1 + \Delta_\chi)}{\delta + \Lambda}, \quad G_{\chi,1} = \frac{\Lambda(1+\delta)\Delta_\chi}{2(\delta + \Lambda)}, \quad G_{\chi,2} = \frac{(1+\delta)\Delta_\chi}{2(\delta+\Lambda)} = \frac{G_{\chi,1}}{\Lambda}. \tag{3.5}$$

3.2 *Perturbed interface*

We introduce a plane wave perturbation of the interface

$$y = \eta(x,t) = \alpha + \epsilon \Re(\mathscr{A} \exp(i(kx - \omega t))), \tag{3.6}$$

with a prescribed real and positive wavenumber k. Here, $\Re$ denotes the real part. The real-order parameter $\epsilon > 0$ is assumed small, so we seek the linear response to the wave disturbance with amplitude $\mathscr{A} = O(1)$. Evolution of the disturbance in time is governed by the imaginary part $\Im(\omega)$ of the generally complex temporal frequency ω. A stable response decays towards zero ($\Im(\omega) < 0$) while unbounded growth ($\Im(\omega) > 0$) characterizes an instability. All other dynamical variables $\Theta \in \{\psi_j, u_j, v_j, p_j, \chi_j\}$ are supposed to develop similar fluctuations, so that

$$\Theta = \Theta(x,y,t) = \Theta^{(0)}(y) + \epsilon \Re(\Theta^{(1)}(y) \exp(i(kx - \omega t))). \tag{3.7}$$

To simplify notation, we identify $\mathscr{D} \equiv \mathrm{d}/\mathrm{d}y$ with the differential operator and further adopt the following definitions:

$$\begin{aligned} k_- &\equiv k(1-\alpha) = \frac{2k\delta}{1+\delta}, \quad k_+ \equiv k(1+\alpha) = \frac{2k}{1+\delta}, \\ c_\xi &\equiv \cosh(k\xi), \quad s_\xi \equiv \sinh(k\xi), \end{aligned} \tag{3.8}$$

where ξ is a dummy variable.

By virtue of the linear field equations (2.4), the stream function perturbations each satisfy

$$(\mathscr{D}^2 - k^2)^2 \psi_j^{(1)} = 0, \tag{3.9}$$

with general solutions of the form

$$\psi_j^{(1)} = (\hat{A}_j + \hat{C}_j y)c_y + (\hat{B}_j + \hat{D}_j y)s_y, \tag{3.10}$$

where $\hat{A}_j$, $\hat{B}_j$, $\hat{C}_j$ and $\hat{D}_j$ are constants to be determined. The linear advection–diffusion law (2.7) yields

$$\left(\mathscr{D}^2 - \left(k^2 + \frac{i}{\mathrm{Cr}\,\Lambda_j}(ku_j^{(0)} - \omega)\right)\right)\chi_j^{(1)} + \frac{ikG_{\chi,j}}{\mathrm{Cr}\,\Lambda_j}\psi_j^{(1)} = 0. \tag{3.11}$$

With constants $\hat{F}_j$ and $\hat{G}_j$, the general solutions

$$\chi_j^{(1)} = \chi_j^{(1)}(y;\omega) = \frac{2\Delta_\chi}{\mathrm{Mg}}((\hat{F}_j\Psi_j + \hat{G}_j\Phi_j) - ikI_j), \tag{3.12}$$

each comprise a complementary function of the independent homogeneous solutions $\Psi_j = \Psi_j(y)$ and $\Phi_j = \Phi_j(y)$, together with a particular integral $I_j = I_j(y; [\psi_j^{(1)}])$. In this general formulation, the Ψ_j and Φ_j are unknown but will be determined explicitly for various cases discussed in Section 4. The I_j are obtained by the variation of parameters method and depend functionally on the flow perturbation:

$$\begin{aligned} I_j &= \hat{A}_j\mathscr{I}_j(y;\ [c_y]) + \hat{B}_j\mathscr{I}_j(y;\ [s_y]) + \hat{C}_j\mathscr{I}_j(y;\ [yc_y]) + \hat{D}_j\mathscr{I}_j(y;\ [ys_y]), \\ \mathscr{I}_j(y;\ [\Xi]) &= \frac{\mathrm{Mg}}{\mathrm{Cr}}\left(\frac{G_{\chi,j}}{2\Delta_\chi\Lambda_j}\right)\int^y \Xi(\xi)\left(\frac{\Psi_j(\xi)\Phi_j(y) - \Psi_j(y)\Phi_j(\xi)}{\mathscr{W}(\Psi_j(\xi),\Phi_j(\xi))}\right)\mathrm{d}\xi, \end{aligned} \tag{3.13}$$

in which

$$\mathscr{W}(\Theta_1(\xi_1),\Theta_2(\xi_2)) = \det\begin{pmatrix} \Theta_1(\xi_1) & \mathscr{D}\Theta_1(\xi_2) \\ \Theta_2(\xi_1) & \mathscr{D}\Theta_2(\xi_2) \end{pmatrix} \tag{3.14}$$

becomes the Wronskian of functions Θ_1 and Θ_2 in case $\xi_1 = \xi_2$. In general, the concentration perturbations $\chi_j^{(1)}$ and the associated quantities in (3.12) will all depend parametrically on the unknown temporal frequency ω.

Substitution of (3.7) into the boundary conditions (2.8–2.10), followed by linearization to lowest order in ϵ obtains

$$\begin{aligned}
&\mathscr{D}\psi_1^{(1)}(-1)=0,\quad \mathscr{D}\psi_2^{(1)}(1)=0, && \text{(no slip on walls)}\\
&\psi_1^{(1)}(-1)=0,\quad \psi_2^{(1)}(1)=0, && \left(\begin{array}{c}\text{stationary, solvent}\\ \text{impermeable walls}\end{array}\right)\\
&\left.\begin{array}{l}\mathscr{D}(\psi_1^{(1)}-\psi_2^{(1)})(\alpha)+J_{\mathbf{u}}\mathscr{A}=0\\ (\psi_1^{(1)}-\psi_2^{(1)})(\alpha)=0\end{array}\right\}, && \left(\begin{array}{c}\text{flow continuity}\\ \text{on interface}\end{array}\right)\\
&k\psi_j^{(1)}(\alpha)+J_\eta\mathscr{A}=0, && \left(\begin{array}{c}\text{moving material}\\ \text{interface}\end{array}\right)\\
&\mathscr{D}(\mathscr{D}^2-3k^2)(\psi_1^{(1)}-\lambda\psi_2^{(1)})(\alpha)-2k^2J_{\perp\sigma}\mathscr{A}=0, && \left(\begin{array}{c}\text{normal stress}\\ \text{balance on interface}\end{array}\right)\\
&(\mathscr{D}^2+k^2)(\psi_1^{(1)}-\lambda\psi_2^{(1)})(\alpha)+2k\left(i\,\mathrm{Mg}\,\frac{\chi_2^{(1)}(\alpha)}{2\varDelta_\chi}+J_{\parallel\sigma}\mathscr{A}\right)=0, && \left(\begin{array}{c}\text{tangential stress}\\ \text{balance on interface}\end{array}\right)\\
&\chi_1^{(1)}(-1)=0,\quad \chi_2^{(1)}(1)=0, && \left(\begin{array}{c}\text{prescribed wall}\\ \text{concentration}\end{array}\right)\\
&(\chi_1^{(1)}-\chi_2^{(1)})(\alpha)+J_\chi\mathscr{A}=0, && \left(\begin{array}{c}\text{concentration continuity}\\ \text{on interface}\end{array}\right)\\
&\mathscr{D}(\chi_1^{(1)}-\varLambda\chi_2^{(1)})(\alpha)=0, && \left(\begin{array}{c}\text{concentration flux}\\ \text{continuity on interface}\end{array}\right)
\end{aligned}\tag{3.15}$$

where the ‘jump’ terms proportional to the interfacial disturbance amplitude $\mathscr{A}$ are

$$\begin{aligned}
J_{\mathbf{u}}&=\mathscr{D}(u_1^{(0)}-u_2^{(0)})(\alpha)=\mathrm{Eu}\,\frac{(1-\lambda)(\lambda-\delta^2)}{\lambda(1+\delta)(\lambda+\delta)},\\
J_\eta&=ku_\alpha^{(0)}-\omega,\\
J_{\perp\sigma}&=\frac{ik}{2},\\
J_{\parallel\sigma}&=i\,\mathrm{Mg}\,\frac{G_{\chi,2}}{2\varDelta_\chi}=i\,\mathrm{Mg}\,\frac{(1+\delta)}{4(\delta+\varLambda)},\\
J_\chi&=G_{\chi,1}-G_{\chi,2}=\frac{(1+\delta)(\varLambda-1)\varDelta_\chi}{2(\delta+\varLambda)}.
\end{aligned}\tag{3.16}$$

The homogeneous linear system (3.15) demands a singular coefficient matrix to deliver non-trivial solutions. Lengthy but straightforward calculation of the determinant leads to the dispersion relation

$$\mathscr{L}_{k,\alpha}(\varLambda)(\kappa_{\mathbf{u}}J_{\mathbf{u}}+\kappa_\eta J_\eta+\kappa_{\perp\sigma}J_{\perp\sigma})+\varLambda\mathscr{L}_{k,\alpha}(1)\kappa_{\parallel\sigma}J_{\parallel\sigma}=0,\tag{3.17}$$

where the function $\mathscr{L}_{k,\alpha}$ and the coefficients $\kappa_{\mathbf{u}}$, κ_η and $\kappa_{\perp\sigma}$ all depend parametrically on ω as detailed in the appendix (Section A.1). The relatively simple coefficient $\kappa_{\parallel\sigma}$ depends only on the wavenumber k and the geometric parameter δ. Further analysis requires solutions of the advection–diffusion equation (2.7) to evaluate the integrals I_j and to determine the functional form of $\mathscr{L}_{k,\alpha}$. As well as the most general case, notable limiting situations are discussed in the following sections.

4. Special cases from the general analysis

4.1 *Case I:* Cr $\to \infty$ *with* $0 < \varLambda < \infty$

For large crispation number and $0 < \varLambda < \infty$, solute diffusion in both films is effectively instantaneous on the time scale of interfacial fluctuations. In this circumstance, the solute transport equation (2.7) then reduces to Laplace's equation and the perturbed concentration fields now satisfy a simple diffusion equation (cf. (3.11))

$$(\mathscr{D}^2 - k^2)\chi_j^{(1)} = 0, \tag{4.1}$$

regardless of any base state flow. Solutions of these homogeneous ODEs take the form (3.12) with

$$\varPsi_j = c_y \quad \text{and} \quad \varPhi_j = s_y, \tag{4.2}$$

independent of ω, and the particular integrals vanish ($I_j = 0$). As a consequence, the concentration fields are decoupled from the fluid flows and can be solved independently to yield

$$\chi_1^{(1)} = -J_\chi \mathscr{A} \frac{k\varLambda c_{1-\alpha} s_{1+y}}{\mathscr{L}_{k,\alpha}^{(0)}(\varLambda)}, \quad \chi_2^{(1)} = J_\chi \mathscr{A} \frac{k c_{1+\alpha} s_{1-y}}{\mathscr{L}_{k,\alpha}^{(0)}(\varLambda)}, \tag{4.3}$$

where

$$\mathscr{L}_{k,\alpha}^{(0)}(\varLambda) = k(\varLambda c_{1-\alpha} s_{1+\alpha} + c_{1+\alpha} s_{1-\alpha}) > 0, \tag{4.4}$$

and the frequency parameter ω does not enter (see the appendix Section A.1). In the case of identical mass diffusivities for both films, then $J_\chi = 0$, so that $\chi_1^{(1)} = \chi_2^{(1)} = 0$, and the base state concentration fields $\chi_j^{(0)}$ are maintained everywhere for all time, regardless of perturbations to the fluid flows.

A dispersion relation of the form (3.17) is obtained:

$$\kappa_{\mathbf{u}}^{(0)} J_{\mathbf{u}} + \kappa_\eta^{(0)} J_\eta + \kappa_{\perp\boldsymbol{\sigma}}^{(0)} J_{\perp\boldsymbol{\sigma}} + \left(\frac{\varLambda \mathscr{L}_{k,\alpha}^{(0)}(1)}{\mathscr{L}_{k,\alpha}^{(0)}(\varLambda)} \right) \kappa_{\parallel\boldsymbol{\sigma}} J_{\parallel\boldsymbol{\sigma}} = 0, \tag{4.5}$$

but where the $\kappa^{(0)}$-coefficients are independent of the frequency parameter ω (see the appendix Section A.1) that now appears only in J_η (see (3.16)). Define the functions

$$g_\xi \equiv \sinh^2(k\xi) - (k\xi)^2, \quad \mathscr{D}g_\xi \equiv \sinh(2k\xi) - 2k\xi, \quad h_\xi \equiv \frac{g_\xi}{\mathscr{D}g_\xi}, \tag{4.6}$$

with a natural extension of our earlier subscript notation (3.8). From (4.5), the disturbance growth rate is

$$
\begin{aligned}
\Im(\omega) &= \frac{\mathscr{L}^{(0)}_{k,\alpha}(\Lambda)\kappa^{(0)}_{\perp\sigma}\Im(J_{\perp\sigma}) + \Lambda\mathscr{L}^{(0)}_{k,\alpha}(1)\kappa_{\parallel\sigma}\Im(J_{\parallel\sigma})}{\mathscr{L}^{(0)}_{k,\alpha}(\Lambda)\kappa^{(0)}_{\eta}} \\
&= \frac{kg_{1+\alpha}}{4\kappa^{(0)}_{\eta}}\left(\mathrm{Mg}\,\mathscr{M}_{k,\alpha}(\Lambda)\left(\lambda\delta^2 - \frac{g_{1-\alpha}}{g_{1+\alpha}}\right) - \mathscr{D}g_{1-\alpha}\left(\lambda + \frac{h_{1-\alpha}}{h_{1+\alpha}}\right)\right) \qquad (4.7)\\
&= \frac{kg_{1-\alpha}}{4\kappa^{(0)}_{\eta}}\lambda\left(\mathrm{Mg}\,\mathscr{M}_{k,\alpha}(\Lambda)\delta^2\left(\frac{g_{1+\alpha}}{g_{1-\alpha}} - \frac{1}{\lambda\delta^2}\right) - \mathscr{D}g_{1+\alpha}\left(\frac{1}{\lambda} + \frac{h_{1+\alpha}}{h_{1-\alpha}}\right)\right),
\end{aligned}
$$

where

$$
\mathscr{M}_{k,\alpha}(\Lambda) = \frac{4k\Lambda\mathscr{L}^{(0)}_{k,\alpha}(1)}{(1+\delta)(\delta+\Lambda)\mathscr{L}^{(0)}_{k,\alpha}(\Lambda)} = \frac{2k_{+}s_2\Lambda}{(\delta+\Lambda)(c_{1-\alpha}s_{1+\alpha}\Lambda + c_{1+\alpha}s_{1-\alpha})} > 0, \qquad (4.8)
$$

depends on the excitation wavenumber, the flow composition and the solute diffusivities, but is a manifestly positive quantity. Similarly, from (4.5), the real part of the temporal frequency is

$$
\begin{aligned}
\Re(\omega) &= ku^{(0)}_{\alpha} + \frac{\kappa^{(0)}_{\mathbf{u}}J_{\mathbf{u}}}{\kappa^{(0)}_{\eta}} \\
&= \frac{\mathrm{Eu}}{\kappa^{(0)}_{\eta}(1+\delta)(\delta+\lambda)}\left(\frac{1}{2}(k_{+}^2\mathscr{D}g_{1-\alpha} + k_{-}^2\mathscr{D}g_{1+\alpha})(\lambda-\delta^2)(\lambda-1) + 2k\kappa^{(0)}_{\eta}\delta\right). \qquad (4.9)
\end{aligned}
$$

Consequences of these results are discussed in Section 6.1.

4.2 *Case II:* $0 < \mathrm{Cr} < \infty$ *and* $\mathrm{Eu} = 0$

In the absence of a driving pressure gradient, the base state is quiescent (note especially that $J_{\mathbf{u}} = 0$, while $J_{\eta} = -\omega$), and the governing equations for the concentration perturbations become

$$
\begin{gathered}
(\mathscr{D}^2 - K_j^2(\omega))\chi_j^{(1)} + \frac{ikG_{\chi j}}{\mathrm{Cr}\,\Lambda_j}\psi_j^{(1)} = 0, \\
\text{where} \quad K_j^2(\omega) = k^2 + K_{0j}^2(\omega) \quad \text{with } K_{0j}^2(\omega) = -\frac{i\omega}{\mathrm{Cr}\,\Lambda_j}.
\end{gathered} \qquad (4.10)
$$

Following our earlier style, the notation is simplified by adopting the definitions

$$
C_{j,\xi} \equiv \cosh(K_j\xi), \qquad S_{j,\xi} \equiv \sinh(K_j\xi). \qquad (4.11)
$$

Although the ODEs (4.10) are inhomogeneous, the coefficients K_j^2 are constant in space, so explicit solutions are readily obtained. The complementary functions comprise

$$
\Psi_j(y) = C_{j,y} \quad \text{and} \quad \Phi_j(y) = S_{j,y}, \qquad (4.12)
$$

with the simple spatially uniform Wronskian $\mathscr{W}(\Psi_j(\xi),\ \Phi_j(\xi)) = K_j(\omega)$. A lengthy but straightforward calculation of the particular integrals leads to the dispersion relation (see the appendix Section A.2)

$$
\mathscr{L}^{(1)}_{k,\alpha}(\Lambda)(-\kappa^{(1)}_{\eta}\omega + \kappa^{(1)}_{\perp\sigma}J_{\perp\sigma}) + \Lambda\mathscr{L}^{(1)}_{k,\alpha}(1)\kappa_{\parallel\sigma}J_{\parallel\sigma} = 0, \qquad (4.13)
$$

where (cf. (4.4))

$$\mathscr{L}^{(1)}_{k,\alpha}(\Lambda) = K_2 \Lambda C_{2,1-\alpha} S_{1,1+\alpha} + K_1 C_{1,1+\alpha} S_{2,1-\alpha}. \tag{4.14}$$

The result (4.13) follows the general form (3.17) but with the Poiseuille flow term absent. As the frequency ω is now intimately incorporated into the arguments of transcendental functions, it is not expedient to explicitly extract the growth rate $\Im(\omega)$ or oscillation rate $\Re(\omega)$ despite the ready availability of (4.13). Nevertheless, implementation of (4.13) (MATLAB, 2013) provides a useful verification tool for other numerical solution schemes (see Section 5.2).

5. General solution

5.1 *Case III:* $0 < \mathrm{Cr} < \infty$ *and* $\mathrm{Eu} \neq 0$

The governing equations for the concentration perturbations become

$$\left(\mathscr{D}^2 - \left(K_j^2(\omega) + \frac{iku_j^{(0)}}{\mathrm{Cr}\,\Lambda_j}\right)\right)\chi_j^{(1)} + \frac{ikG_{\chi,j}}{\mathrm{Cr}\,\Lambda_j}\,\psi_j^{(1)} = 0, \tag{5.1}$$

where $u_j^{(0)}$ is quadratic in y as given by (3.2). In the base state, the parabolic velocity profiles of (3.2) share a common symmetry axis located at (see Fig. 2)

$$y = \bar{y} = \frac{\delta(1-\lambda)}{(1+\delta)(\delta+\lambda)}. \tag{5.2}$$

On applying the transformation

$$Y(y) = \left(\frac{2ik\,\mathrm{Eu}}{\mathrm{Cr}\,\Lambda_j}\right)^{1/4}(y-\bar{y}), \tag{5.3}$$

the homogeneous equation corresponding to (5.1) is brought into the standard form

$$\left(\frac{\mathrm{d}^2}{\mathrm{d}Y^2} + \left(\frac{1}{4}Y^2 - \Upsilon_j(\omega)\right)\right)\chi_j^{(1)} = 0, \tag{5.4}$$

where

$$\Upsilon_j(\omega) = \left(K_j^2(\omega) + \frac{ik\bar{u}_j^{(0)}}{\mathrm{Cr}\,\Lambda_j}\right)\left(\frac{2ik\,\mathrm{Eu}}{\mathrm{Cr}\,\Lambda_j}\right)^{-1/2}, \tag{5.5}$$

and we have the complementary solution in terms of a single parabolic cylinder (Weber) function (Abramowitz & Stegun, 1965)

$$\Psi_j(y) = W(\Upsilon_j, y) \quad \text{and} \quad \Phi_j(y) = W(\Upsilon_j, -y), \tag{5.6}$$

with the constant Wronskian $\mathscr{W} = 1$. These analytic solutions of the transport equations (5.1) lead to a very complicated implicit dispersion relation involving transcendental functions. It appears very difficult (if not impossible) to exactly solve this eigenvalue problem, or merely to establish precisely how many response modes exist. Here, we shall consider a numerical scheme, instead, that will resolve these issues.

5.2 *A numerical scheme: Chebyshev collocation method*

Recall that the stream function perturbations $\psi_j^{(1)}$ satisfy a biharmonic field equation (3.9), that is equivalent to the Orr–Sommerfeld equation at vanishing Reynolds number, and explicit solutions are obtained in the form (3.10). Following Gottlieb & Orszag (1977), the set of orthogonal Chebyshev polynomials $T_n : [-1, 1] \to [-1, 1]$ provides an appropriate basis for the approximation space of $\chi_j^{(1)}$, and we write the truncated expansions

$$\chi_j^{(1)}(y) = \sum_{n=0}^{N_j} a_{jn} T_n(y_j(y)), \tag{5.7}$$

where the spanwise coordinate is linearly mapped onto the canonical domain:

$$\begin{aligned} y_1(y) &= (1+\delta)y + \delta, \quad (-1 \leqslant y \leqslant \alpha), \\ y_2(y) &= \frac{1}{\delta}((1+\delta)y - 1), \quad (\alpha \leqslant y \leqslant 1), \end{aligned} \tag{5.8}$$

with the differential transformations

$$\mathscr{D}y_1 = 1 + \delta \quad \text{and} \quad \mathscr{D}y_2 = 1 + \frac{1}{\delta}. \tag{5.9}$$

The Gauss–Lobatto points

$$y_{jn} = \cos\left(\frac{n\pi}{N_j}\right), \quad (n = 0, 1, 2, \ldots, N_j) \tag{5.10}$$

corresponding to the extrema of the highest order polynomial, are optimal for collocation (Schmid & Henningson, 2001). Altogether with the linearized boundary conditions (3.15), this set of governing equations is assembled into the system

$$\mathbf{A}\mathbf{w} = \omega \mathbf{B}\mathbf{w}, \tag{5.11}$$

which we recognize as a generalized eigenvalue problem for the eigenvalue ω and the associated eigenvector

$$\mathbf{w} = \begin{pmatrix} a_{10} & \ldots & a_{1N_1} & a_{20} & \ldots & a_{2N_2} & \hat{A}_1 & \hat{B}_1 & \hat{C}_1 & \hat{D}_1 & \hat{A}_2 & \hat{B}_2 & \hat{C}_2 & \hat{D}_2 & \mathscr{A} \end{pmatrix}^\top. \tag{5.12}$$

These $N_1 + N_2 + 11$ unknowns are determined by the 13 boundary conditions along with the field evaluations at the $(N_1 - 1) + (N_2 - 1)$ 'interior' collocation points corresponding to the turning points of T_{N_1} and T_{N_2}. A Matlab code (MATLAB, 2013) has been implemented using the built-in routine `eig` to solve the generalized eigenvalue problem. To consistently compare results across the wavenumber spectrum, the eigenvectors are uniformly scaled, so that the disturbance amplitude of the interface becomes $\mathscr{A} = 1 \in \mathbb{R}$.

5.3 *The situation* $k = 0$ *and* $\mathrm{Eu} \geqslant 0$

At zero wavenumber, it turns out that a base state flow plays no role in the eigenvalue spectrum. The governing equations (3.9) for the stream function perturbations reduce to

$$\mathscr{D}^4 \psi_j^{(1)} = 0, \tag{5.13}$$

with general solutions in the form of a cubic polynomial

$$\psi_j^{(1)} = \hat{A}_j y^3 + \hat{B}_j y^2 + \hat{C}_j y + \hat{D}_j. \tag{5.14}$$

The concentration field perturbations are also determined by homogeneous ODEs

$$(\mathscr{D}^2 - K_{0j}^2(\omega))\chi_j^{(1)} = 0, \tag{5.15}$$

with general solutions (cf. (3.12))

$$\chi_j^{(1)} = \frac{2\Delta_\chi}{\mathrm{Mg}}(\hat{F}_j C_{j,y} + \hat{G}_j S_{j,y}). \tag{5.16}$$

Furthermore, the interfacial stress boundary conditions are simplified considerably: in particular, the tangential coupling between $\psi_j^{(1)}$ and $\chi_j^{(1)}$ is broken, so that the dispersion relation is easily recovered:

$$\omega \mathscr{L}_{0,\alpha}^{(1)}(\Lambda) \left(\frac{\lambda^2 + 2\delta(2\delta^2 + 3\delta + 2)\lambda + \delta^4}{(1+\delta)^4} \right) = 0, \tag{5.17}$$

and the non-trivial modes are determined by (cf. (4.14))

$$\mathscr{L}_{0,\alpha}^{(1)}(\Lambda) = K_0(\sqrt{\Lambda} \cosh(K_0 h_-) \sinh(K_0 h_+) + \cosh(K_0 h_+) \sinh(K_0 h_-)) = 0, \tag{5.18}$$

where

$$h_- = \frac{2\delta}{(1+\delta)\sqrt{\Lambda}} = \frac{1-\alpha}{\sqrt{\Lambda}}, \quad h_+ = \frac{2}{1+\delta} = 1 + \alpha \quad \text{and} \quad K_0 = \sqrt{-\frac{i\omega}{\mathrm{Cr}}}. \tag{5.19}$$

6. Results and discussion

6.1 *Instantaneous solute diffusion* $\mathrm{Cr} \to \infty$, $0 < \Lambda < \infty$ *(Case I)*

Explicit expressions for the temporal frequency in Case I (4.7) and (4.9) permit detailed analysis of the linear response. For all physical parameter values, the quantity $\kappa_\eta^{(0)}$ is strictly positive (see the appendix Section A.3). It follows from (4.7) that the interface is generally stable ($\Im(\omega) < 0$) against large wavenumber perturbations ($k \to \infty$). By considering the k-expansion

$$\Im(\omega) = \frac{\mathrm{Mg}(\lambda - \delta^2)\Lambda\delta^2}{(\lambda^2 + 2\delta(2 + 3\delta + 2\delta^2)\lambda + \delta^4)(\Lambda + \delta)^2} k^2 + O(k^4), \tag{6.1}$$

a region of instability exists for $\mathrm{Mg} > 0$, provided $\lambda > \delta^2$. Conversely, $\mathrm{Mg} < 0$ requires $\lambda < \delta^2$ for this instability to appear. Hence, it is natural to define a *pseudo*-critical viscosity ratio $\lambda_c = \delta^2$. It should be emphasized here that this is a small wavenumber analysis that does not exclude the possibility of instabilities where $\Im(\omega)$ first becomes positive for some wavenumber $k_c > 0$.

These response characteristics are confirmed by the family of dispersion curves plotted in Fig. 3 where, given $\mathrm{Mg} = 100$, panels (a–c) consistently exhibit a stable response for $\lambda > \delta^2$, a marginal state at $\lambda = \delta^2$ and instability for $\lambda < \delta^2$. Within the systematic classification scheme of Cross and co-workers (Cross & Hohenberg, 1993; Cross & Greenside, 2009), this is a stationary instability of type II universally characterized by a zero growth rate at $k = 0$ and maximum amplification rate at intermediate wavenumber $0 < k < \infty$. Figure 3 also demonstrates that the stability criterion is independent of the mass diffusivity ratio $\varLambda$. This is unsurprising in the limit ($\mathrm{Cr} \to \infty$), since equilibration of the concentration profile is fast compared with the flow dynamics: the interface moves in a concentration field that is oblivious to the fluid flows. Despite this decoupling, the concentration field is perturbed nevertheless (see (4.3)) by a stratification of the bulk mass diffusivity (Fig. 3(d)). Throughout Fig. 3, the analytic results (Section 4.1) show excellent agreement with the approximate collocation computations (Section 5.2).

For arbitrary wavenumber, marginal stability relations ($\Im(\omega) = 0$) are obtained directly from (4.7), and solving for the interfacial elasticity parameter yields

$$\mathrm{Mg}_0 = \frac{g_{1+\alpha}\mathscr{D}g_{1-\alpha}\lambda_0 + g_{1-\alpha}\mathscr{D}g_{1+\alpha}}{\mathscr{M}_{k,\alpha}(\varLambda)(g_{1+\alpha}\delta^2\lambda_0 - g_{1-\alpha})} = \frac{g_{1+\alpha}\mathscr{D}g_{1-\alpha} + g_{1-\alpha}\mathscr{D}g_{1+\alpha}\lambda_0^{-1}}{\mathscr{M}_{k,\alpha}(\varLambda)(g_{1+\alpha}\delta^2 - g_{1-\alpha}\lambda_0^{-1})}, \tag{6.2}$$

where Mg_0 and λ_0 are marginal values of the corresponding control parameters. This is a special case of the result first obtained by Smith (1966) (see the appendix, Section A.4) for the analogous thermocapillary situation, but where a neutral stability criterion was imposed *before* solving the eigenvalue problem. Equations (6.2) describe rectangular hyperbolae, centred on a point denoted by $\mathscr{C}_{k,\alpha}^{(+)}$ in the $(\lambda_0,\ \mathrm{Mg}_0)$ plane, or centred on $\mathscr{C}_{k,\alpha}^{(-)}$ in the $(\lambda_0^{-1},\ \mathrm{Mg}_0)$ plane with coordinates

$$\mathscr{C}_{k,\alpha}^{(+)} = \left(\frac{1}{\delta^2}\left(\frac{g_{1-\alpha}}{g_{1+\alpha}}\right),\ \frac{\mathscr{D}g_{1-\alpha}}{\delta^2\mathscr{M}_{k,\alpha}(\varLambda)}\right) \quad \text{and} \quad \mathscr{C}_{k,\alpha}^{(-)} = \left(\delta^2\left(\frac{g_{1+\alpha}}{g_{1-\alpha}}\right),\ -\frac{\mathscr{D}g_{1+\alpha}}{\mathscr{M}_{k,\alpha}(\varLambda)}\right). \tag{6.3}$$

Since g is both positive and strictly increasing (see definitions (4.6)), it is easy to verify

$$\begin{gathered} 0 < \delta < 1 \ \Rightarrow\ 0 < \alpha < 1 \ \Rightarrow\ \delta^4 < \frac{g_{1-\alpha}}{g_{1+\alpha}} < 1, \\ 1 < \delta < \infty \ \Rightarrow\ -1 < \alpha < 0 \ \Rightarrow\ \frac{1}{\delta^4} < \frac{g_{1+\alpha}}{g_{1-\alpha}} < 1 \\ \text{and} \quad \lim_{k \to \infty} \frac{\mathscr{D}g_{1\pm\alpha}}{\mathscr{M}_{k,\alpha}(\varLambda)} \exp(-2k_\pm) = 0, \end{gathered} \tag{6.4}$$

so that the positions $\mathscr{C}_{k,\alpha}^{(\pm)}$ are restricted as shown in Fig. 4. It follows that global temporal stability is confined to the λ_0 axis (where $\mathrm{Mg}_0 = 0$) and either the region $(\lambda_0,\ \mathrm{Mg}_0) \in (0,\ \delta^2) \times (0,\ \infty)$ for $0 < \delta \leqslant 1$, or the region $(\lambda_0^{-1},\ \mathrm{Mg}_0) \in (0,\ \delta^2) \times (-\infty,\ 0)$ for $1 \leqslant \delta$. This is consistent with the small wavenumber analysis and confirms the critical viscosity ratio $\lambda_c = \delta^2$. With a more conventional insoluble surfactant ansatz, the same result has been established in the small-k analysis of Frenkel & Halpern (2002) and the lubrication-flow model of Blyth & Pozrikidis (2004a). A similar asymptotic analysis reported by Merkt *et al.* (2005) has also obtained stability diagrams (their Fig. 4) consistent with Fig. 4.

A mechanical interpretation of this small wavenumber instability is illustrated in Fig. 5. Merkt *et al.* (2005) have also discussed a similar mechanism in the context of competition between capillary action and the Rayleigh–Taylor instability for systems with mass density stratification. Large-scale

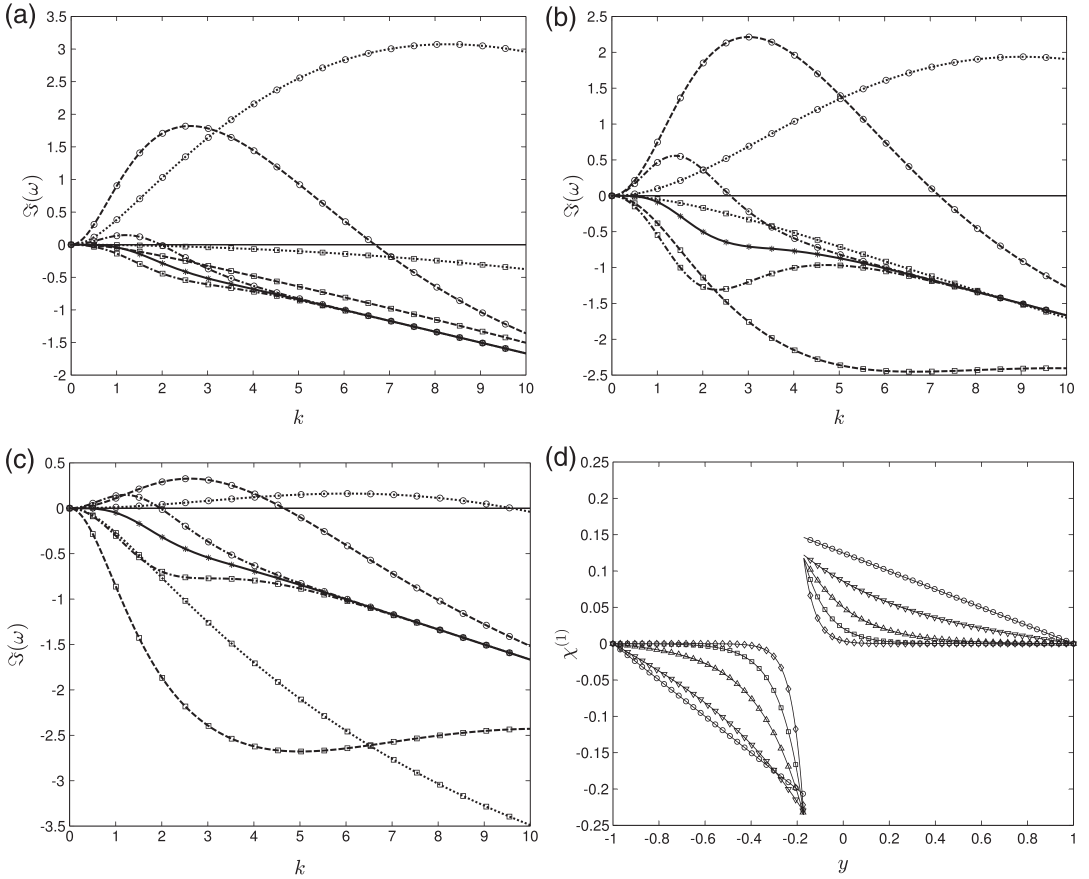

FIG. 3. Growth rate dispersion curves for Case I ($\mathrm{Cr} \to \infty$) are displayed for parameter values $\mathrm{Mg} = 100$, $\lambda = 2$ and $\varDelta_\chi = 1$ with (a) $\varLambda = 0.1$; (b) $\varLambda = 1$ and (c) $\varLambda = 10$. Results from the analytic expression (4.7), shown as lines, are compared with isolated point calculations using the numerical collocation method (denoted by symbols) described in Section 5.2 with $N_1 = N_2 = 32$. Entirely stable response is indicated by squares with the flow composition parameter δ set to $40(\cdot\cdot\cdot)$, $10(--)$ and $2(\cdot-\cdot)$. Circles identify response curves showing the small wavenumber instability with δ set to $1(\cdot-\cdot)$, $0.2(--)$ and $0.05(\cdot\cdot\cdot)$. The marginally stable response is plotted with asterisk symbols and a solid line (——) where $\delta_c = \sqrt{\lambda} = \sqrt{2}$. At the stability margin ($\lambda = 2$ and $\delta = \sqrt{2}$ with $\mathrm{Mg} = 100$, $\varDelta_\chi = 1$ and $\varLambda = 2$), panel (d) shows a corresponding comparison of concentration perturbation profiles across the slab where results from (4.3) are plotted as lines and collocation calculations are denoted by symbols with wavenumbers k set to 0.1(◯), 2(▽), 5(△), 10 (☐) and 20(◇).

disturbances are suppressed by a destructive normal fluid velocity component with a π phase shift (Fig. 5(a,b)), whereas changes in γ remain in-phase with the interface profile. At the margin of stability (Fig. 5(c,d)) $v^{(1)}(y)$ swaps, on passing through the interface, from constructive in-phase to destructive out-of-phase interference with the disturbance wave. An unstable response is characterized by an in-phase normal velocity component that amplifies the interfacial disturbance (Fig. 5(e,f)). In steady Stokes flow, the vorticity

$$\boldsymbol{\varpi}_j = \nabla \times \mathbf{u}_j = \left(\frac{\partial v_j}{\partial x} - \frac{\partial u_j}{\partial y}\right)\mathbf{k} = -\nabla^2 \psi_j \mathbf{k}, \tag{6.5}$$

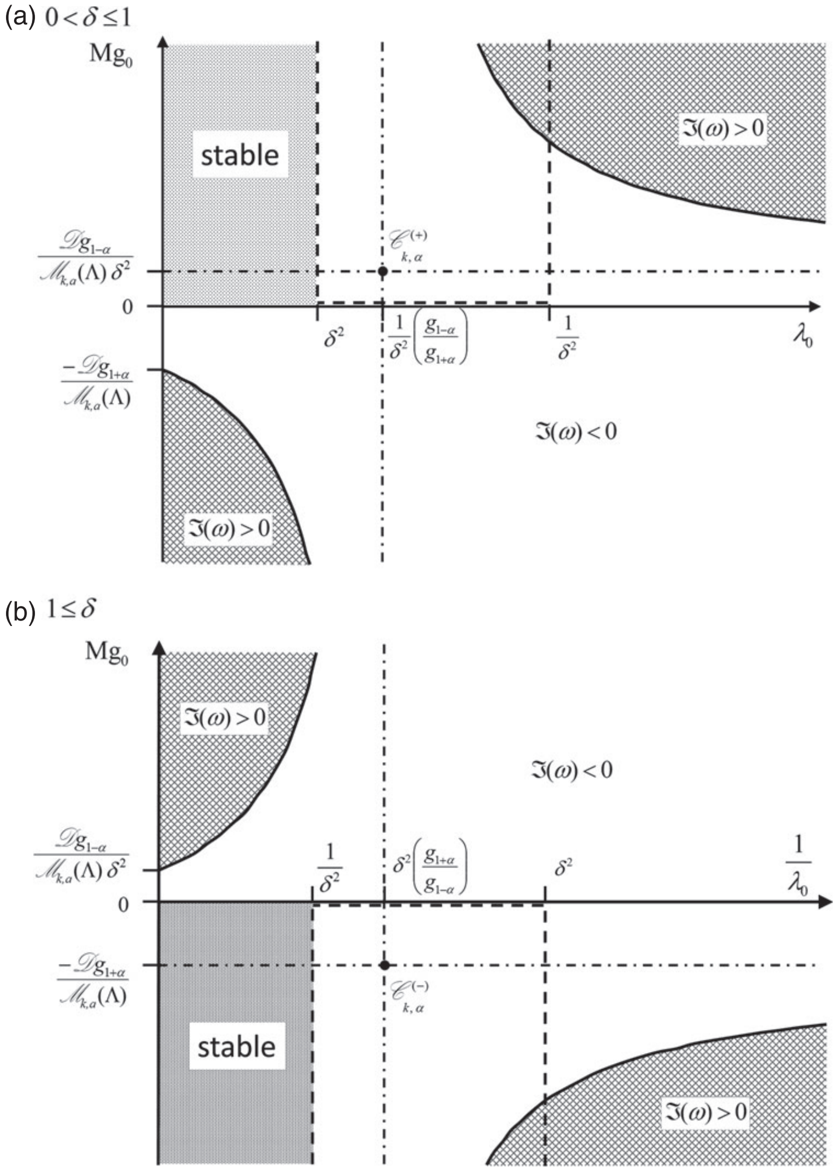

FIG. 4. Stability diagram for Case I ($\mathrm{Cr}\to\infty$ and $0<\Lambda<\infty$). Typical marginal stability boundaries ($\Im(\omega)=0$) projected into the plane of viscosity ratio λ_0 and Gibbs elasticity Mg_0 appear as a rectangular hyperbola (——). With varying excitation wavenumber k, the asymptotes ($\cdot - \cdot$) move about the plane but the centre $\mathscr{C}^{(\pm)}_{k,\alpha}$ is confined to the unbounded rectangular region indicated as ($--$). Provided $\lambda_0<\lambda_c=\delta^2$, a domain of stability (shaded area) can be identified where all linear perturbations decay in time.

is harmonic $\nabla^2\boldsymbol{\varpi}_j=\mathbf{0}$ (cf. (2.4)) and closely related to the pressure so that $\lambda_j(\partial\boldsymbol{\varpi}_j/\partial x)=(\partial p_j/\partial y)\mathbf{k}$ and $\lambda_j(\partial\boldsymbol{\varpi}_j/\partial y)=(\partial p_j/\partial x)\mathbf{k}$. Consequently, the vorticity is discontinuous at the interface and the phase of the perturbation $\mathrm{Arg}(\varpi^{(1)})$ changes abruptly at $y=\alpha$ from a $\pi/2$ lag in the more viscous film to a

$\pi/2$ lead in the less viscous layer (Fig. 5(b,d,f)). It appears that the pressure is always destructively out of phase with the interface deformation over the whole fluid slab (data not shown). Although four convection cells are evident in the marginal state (Fig. 5(c,d)), only two cells develop for states lying deep in either the stable (e.g. Fig. 5(a,b)) or unstable (data not shown) regimes. This contrasts with several studies of the analogous thermocapillary problem (Andereck *et al.*, 1998) that focused on different flow patterns, but where four cells are always generated by imposing a rigid undeformable interface.

In this special Case I, only a single response mode is excited that always remains completely decoupled from the base state flow: the growth rate $\Im(\omega)$ given by (4.7) is independent of Eu. For a quiescent base state flow the disturbance is, of course, stationary in space ($\Re(\omega)=0$), but if a pressure gradient exists ($\mathrm{Eu}>0$) it can be deduced from (4.9) that $\Re(\omega)>0$ (see the appendix Section A.5) and a propagating wave develops on the interface that travels downstream with the speed

$$\begin{aligned}\frac{\Re(\omega)}{k} &= u_{\alpha}^{(0)} + \frac{\kappa_{\mathbf{u}}^{(0)} J_{\mathbf{u}}}{k\kappa_{\eta}^{(0)}} \\ &= \frac{\mathrm{Eu}}{\kappa_{\eta}^{(0)}(1+\delta)(\delta+\lambda)}\left(\left(\frac{k_{+}^{2}\mathscr{D}g_{1-\alpha}+k_{-}^{2}\mathscr{D}g_{1+\alpha}}{k_{+}+k_{-}}\right)(\lambda-\delta^{2})(\lambda-1)+2\kappa_{\eta}^{(0)}\delta\right). \qquad (6.6)\end{aligned}$$

Further, setting $\mathrm{Eu}=\frac{1}{2}(1+\delta)(\delta+\lambda)/\delta$, or equivalently demanding the horizontal fluid velocity component satisfies $u_{\alpha}^{(0)}=1$, and also choosing $\delta=1$ before finally considering the limit $k\to\infty$, we recover the dispersionless result

$$\frac{\Re(\omega)}{k} = 1 + \frac{2(1-\lambda)^{2}}{\lambda^{2}+14\lambda+1}, \qquad (6.7)$$

obtained by Yih (1967) for the plane Poiseuille flow in a finite channel of two superposed fluids with equal depth and density, but different viscosities.

6.2 *Comparable diffusion rates of matter and momentum* $0<\mathrm{Cr}<\infty$ *(Case II)*

At finite crispation numbers (Cases II and III), the response behaviour is qualitatively very different (see Fig. 6 for example) from Case I (Section 6.1). Analysis of the $k=0$ situation (see the appendix Section A.6) shows that the temporal frequency has zero real part ($\Re(\omega)=0$) and non-positive imaginary part ($\Im(\omega)\leqslant 0$). Indeed, the dispersion relation (5.18) reduces to

$$\sqrt{\Lambda}\sin\left(h_{+}\sqrt{-\frac{\Im(\omega)}{\mathrm{Cr}}}\right)\cos\left(h_{-}\sqrt{-\frac{\Im(\omega)}{\mathrm{Cr}}}\right)+\cos\left(h_{+}\sqrt{-\frac{\Im(\omega)}{\mathrm{Cr}}}\right)\sin\left(h_{-}\sqrt{-\frac{\Im(\omega)}{\mathrm{Cr}}}\right)=0. \qquad (6.8)$$

Formally, this defines the nodes of a wave with two harmonic components differing in both frequency and amplitude described by

$$(\sqrt{\Lambda}+1)\sin\left(\frac{2}{1+\delta}\left(1+\frac{\delta}{\sqrt{\Lambda}}\right)\sqrt{-\frac{\Im(\omega)}{\mathrm{Cr}}}\right)+(\sqrt{\Lambda}-1)\sin\left(\frac{2}{1+\delta}\left(1-\frac{\delta}{\sqrt{\Lambda}}\right)\sqrt{-\frac{\Im(\omega)}{\mathrm{Cr}}}\right)=0. \qquad (6.9)$$

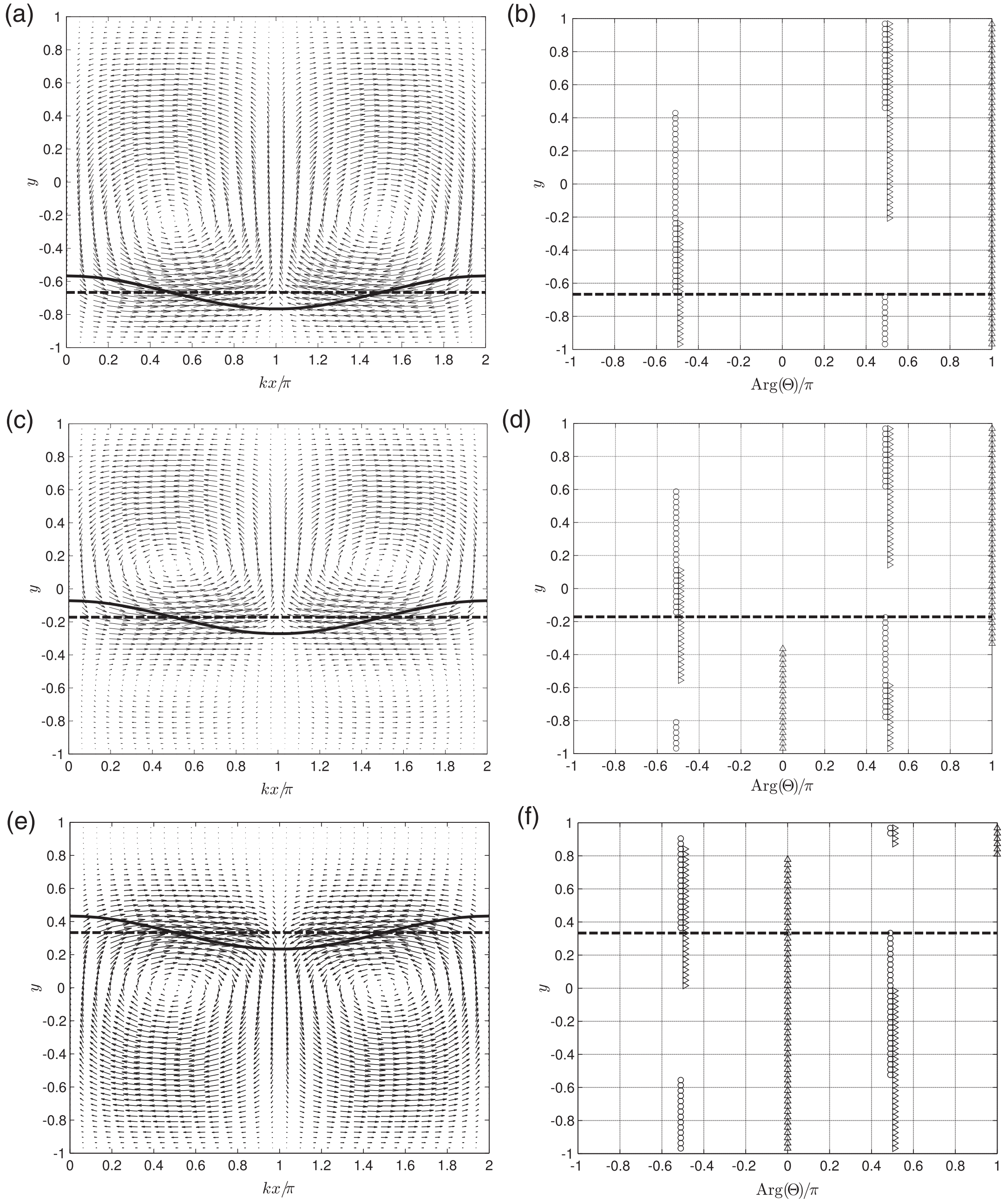

FIG. 5. Flow fields calculated by the collocation method ($N_1 = N_2 = 32$) are shown for Case I with $\mathrm{Cr} \to \infty$. Throughout, the control parameter values $\mathrm{Mg} = 5$, $\mathrm{Eu} = 0$, $\lambda = 2$, $\Lambda = 1$, $\Delta_\chi = 1$ are set. Panels (a), (c) and (e): direction fields associated with the fluid velocity $\mathbf{u}(x, y) = u(x, y)\mathbf{i} + v(x, y)\mathbf{j}$ are plotted. The superimposed lines indicate the quiescent interface position (−−) and a harmonic disturbance (—–) of arbitrary amplitude ($\epsilon = 0.1$). Panels (b), (d) and (f): show the corresponding principal arguments of the perturbed velocities and vorticity field $\Theta \in \{u^{(1)}(y),\ v^{(1)}(y),\ \varpi^{(1)}(y)\}$. The tangential $u^{(1)}$ and normal $v^{(1)}$ velocity components are denoted by ($\triangleright$) and ($\triangle$), respectively, and the phase of the vorticity $\varpi^{(1)}$ is indicated by ◯. Again, the quiescent interface position is shown by (−−). Each pair of panels indicates a stable situation ($\delta = 5$, a and b); a marginal situation ($\delta = \sqrt{2}$, c and d) and an unstable situation ($\delta = 0.5$, e and f).

A general closed form solution of (6.9) is intractable. If $\varLambda = 1$, however, the second term vanishes in (6.9) and a simple expression, independent of δ, is obtained for the growth rate spectrum

$$\sqrt{-\frac{\Im(\omega)}{\mathrm{Cr}}} = m\frac{\pi}{2}, \quad (m = 0, 1, 2, \ldots). \tag{6.10}$$

Similarly, if $\varLambda = \delta^2$, then

$$\frac{1}{1+\delta}\sqrt{-\frac{\Im(\omega)}{\mathrm{Cr}}} = m\frac{\pi}{4}, \quad (m = 0, 1, 2, \ldots). \tag{6.11}$$

In both these special situations, the mode spacing is proportional to $(2m+1)\mathrm{Cr}$. More generally, expansion of (6.9) to order $\mathrm{Cr}^{-3/2}$ demonstrates that the first harmonic ($m = 1$) is always shifted from the fundamental ($m = 0$) by an amount proportional to Cr. This is consistent with the finding from Case I ($\mathrm{Cr} \to \infty$) where only the single $m = 0$ response remains and all other modes have retreated to infinity.

Figure 6(a) compares Case II growth rate dispersion curves at control parameter values corresponding to a stable Case I response: $\lambda = 2$ and $\delta = \sqrt{40} > \sqrt{\lambda}$ with $\mathrm{Mg} = 100$, $\varLambda = 1$ and $\varDelta_\chi = 1$ (Fig. 3(b)). For $\mathrm{Cr} \geqslant 1$, the dominant mode is stable and qualitatively similar to the Case I situation. The most obvious departure from Case I is the appearance of multiple lower lying modes whose character and interactions sensitively depend on control parameters other than viscosity ratio λ and geometry δ. In particular, at $\mathrm{Cr} = 1$, an avoided crossing is evident between the fundamental and the first harmonic, but for larger crispation number the two highest stationary modes pass through an exceptional point where a pair of spatially propagating waves are excited that travel in opposite directions with phase velocities of equal magnitude. There is also evidence in Fig. 6(a) of a second exceptional point at higher wavenumber ($k \approx 4$) where the superposed response splits back to two standing wave modes with distinct temporal decay rates. Moreover, at $\mathrm{Cr} = 50$ (see inset of Fig. 6(a)), the combined oscillatory mode exhibits an *instability* of type I in the classification by Cross and co-workers (Cross & Hohenberg, 1993; Cross & Greenside, 2009). In contrast with type II behaviour, type I is characterized by the onset of instability at a *non-zero* wavenumber. For standing wave modes, Fig. 6(a) also includes direct numerical solutions of the dispersion relation (4.13) obtained with the Matlab `fsolve` routine using the Levenberg–Marquardt algorithm (Fan, 2003). The excellent agreement serves again to verify both the analysis and the collocation method implementation. Conversely, at parameter values corresponding to an unstable response in Case I, ($\lambda = 2$, $\delta = 1/\sqrt{10}$, $\mathrm{Mg} = 20$, $\varLambda = 1$, $\varDelta_\chi = 1$) increasing the interfacial tension has a stabilising effect and reduces the maximum temporal growth rate as shown in Fig. 6(b). The diversity of response behaviour is also apparent here with multiple splittings between states having either monotone or oscillatory time dependence in the decay rate. Excitation of spatially propagating waves is confirmed in Fig. 6(c) where non-zero $\Re(\omega)$ appears and coincides with the linear superposition of two modes to form a stationary solution in space that oscillates in time. At very high interfacial tension ($\mathrm{Cr} = 0.0002$), an unstable oscillatory response can be observed as shown in Fig. 6(d). An example of mode *exchange* is also apparent ($k \approx 3$) where a single stationary mode emerges to dominate a standing wave pair without passing through an exceptional point.

The previously noted (Fig. 6(a)) avoided-crossing or level-repulsion phenomenon (Lax, 2007) is linked with the likelihood that a given operator has eigenvalues with non-trivial algebraic multiplicity (Betcke & Trefethen, 2004). Figure 7(a) examines the effect more closely where, at fixed interfacial tension $\mathrm{Cr} = 0.1$, growth rate dispersion curves are plotted for $5 \leqslant \mathrm{Mg} \leqslant 100$ with $\mathrm{Eu} = 0$, $\delta = \lambda = 2$, $\varLambda = 1$ and $\varDelta_\chi = 1$. As the interfacial elasticity increases, two distinct avoiding modes approach more

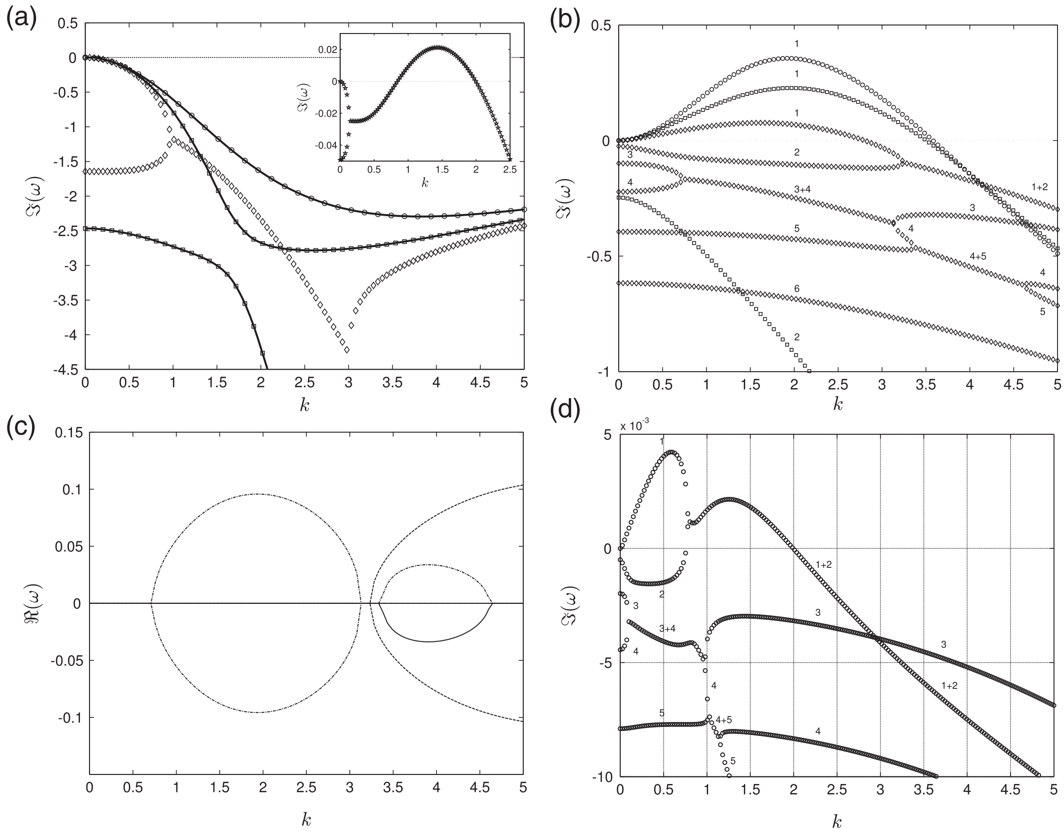

FIG. 6. Temporal frequency dispersion curves $\omega = \omega(k)$ are shown for a fluid slab of uniform mass diffusivity ($\Lambda = 1$) and unit concentration difference on the bounding walls ($\Delta_\chi = 1$). Panel (a): at $\mathrm{Mg} = 100$, the growth rate $\Im(\omega)$ is compared between Case I ($\mathrm{Cr} \to \infty$) (◯) and Case II ($\mathrm{Eu} = 0$) with finite Cr set to 1(□), 1.5(◇) and 50(⋆), all obtained by the collocation method (Section 5.2). Other control parameters are $\lambda = 2$ and $\delta = \sqrt{40} > \sqrt{\lambda}$ corresponding to a stable response in Case I. Solid lines correspond to evaluation of the explicit result (4.7) in Case I, and to numerical solutions of the dispersion relation (4.13) in Case II. Panel (b): at $\mathrm{Mg} = 20$, the growth rate $\Im(\omega)$ is compared between Case I ($\mathrm{Cr} \to \infty$) (◯) and Case II ($\mathrm{Eu} = 0$) with finite Cr set to 0.1(□) and 0.01(◇), all obtained by the collocation method (Section 5.2). Other control parameters are $\lambda = 2$ and $\delta = 1/\sqrt{10} < \sqrt{\lambda}$ corresponding to an unstable response in Case I. Modes are identified by number and oscillatory responses are indicated by linear superposition of stationary states between a pair of exceptional points. Panel (c): the spatially propagating wave frequencies $\Re(\omega)$ are shown, corresponding to the data of panel (b) for $\mathrm{Cr} = 0.01$. Modes are identified as follows: 1 and 2 (−−); 3 and 4 (· − ·); and 5 (——). Panel (d): shows the growth rate $\Im(\omega)$ dispersion curves, obtained by the collocation method (Section 5.2), in a situation where mass diffusion is extremely slow $\mathrm{Cr} = 0.0002$. Other control parameters are set as in panel (b). Modes are identified by number. An unstable oscillatory state is observed ($k < 1$) as well as a dominant mode exchange crossing at $k \approx 3$.

and more closely at $k \approx 2$, then merge at a single point near $\mathrm{Mg} = 7.35$ that subsequently decomposes into a pair of exceptional points at higher Mg.

Seyranian *et al.* (2005) have reported a theory of strong coupling between eigenvalues of a complex valued matrix with respect to the smooth variation of parameters upon which the coefficients depend. In a finite-dimensional vector space, an exceptional point (Kato, 1980) arises where two eigenvalues coalesce to give an algebraic multiplicity of 2, but a smaller geometric multiplicity of 1. Thus, the

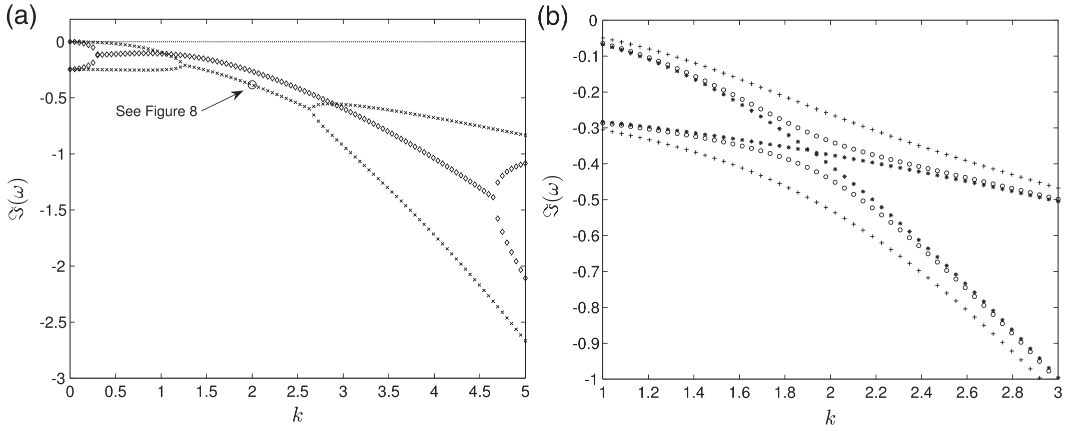

FIG. 7. Collapse of avoided crossing between stationary modes to form an oscillatory mode with increasing interfacial elasticity is illustrated. Growth rate dispersion curves $\Im(\omega(k))$ are plotted in panel (a) for Mg set to 5(+), 7(□), and in panel (b) for Mg set to 7.35(⋆), 10(×) and 100(◇). Other control parameters are $\mathrm{Ca} = 0.1$, $\mathrm{Eu} = 0$, $\delta = \lambda = 2$, $\Lambda = 1$ and $\Delta_\chi = 1$.

corresponding eigenvectors also merge, becoming linearly dependent and forming a non-trivial Jordan block that renders the underlying matrix defective (not diagonalizable over $\mathbb{C}$). In the situation where only a single parameter is varied (the wavenumber k for example), the two eigenvalues collide with infinite 'speed' (the derivative with respect to the parameter is unbounded) and subsequently diverge in the perpendicular direction with a complete loss of information on the relationship before and after strong coupling (Seyranian *et al.*, 2005). This phenomenon is entirely consistent with the observed behaviour (Fig. 6(a) with $\mathrm{Cr} = 1.5$, for instance) of mode coupling between independent stationary and combined oscillatory states. Furthermore, the theory of Seyranian *et al.* (2005) explains characteristic properties of singularities in the surfaces representing complex resonance energy eigenvalues of quantum systems (Hernández *et al.*, 2003) that are manifest as level repulsion in the real and imaginary parts. It remains unclear how the details of this analysis relate to avoided crossings and mode exchanges of $\Im(\omega)(k)$ in stationary states where $\Re(\omega) = 0$.

In the absence of a bulk buoyancy mechanism, and allowing for distortion of the interface, counter-rotating fluid cells are consistently observed in the stationary states (see Fig. 5, for example) but the oscillatory standing wave state periodically changes the sense of rotation. The temporal evolution of this pattern is illustrated in Fig. 8 by snapshots of the fluid velocity direction field over one cycle. The corresponding interfacial disturbance is also indicated and shows that the flow reversal is associated with instants where the interface adopts its unperturbed flat profile. Note that, for clarity here, the exponential decay of the disturbance in this stable response has been artificially suppressed where the spatial amplitude would otherwise be damped out within a fraction of one temporal cycle.

6.3 *Effect of base state flow* $\mathrm{Eu} > 0$ *(Case III)*

Figure 9(a) demonstrates the effect of a base state flow in a relatively simple situation with no mode interaction (cf. Fig. 6(b)). The growth rates of instabilities are enhanced with increasing Eu, whereas a stable response is further suppressed. For the particular parameter set corresponding to Fig. 6(b), which is unstable in Case I, with $\mathrm{Cr} = 0.1$, it appears that the marginal stability boundary is not sensitive to changes in base state flow. At the interface, a spatially propagating wave is excited that always moves

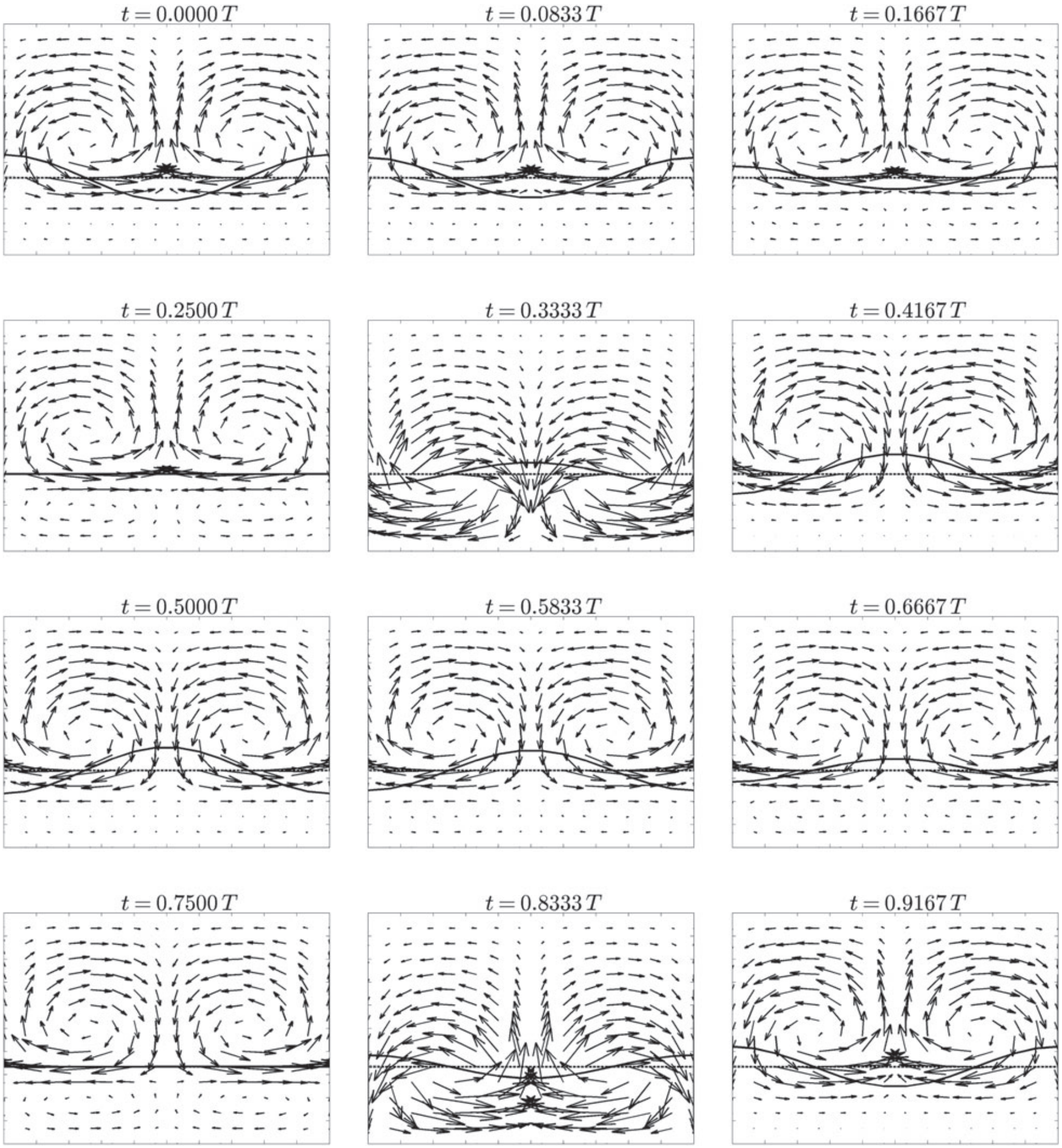

FIG. 8. Temporal evolution of flow pattern in the oscillatory state (identified in Fig. 7 at parameter values, $\mathrm{Cr} = 0.1$, $\mathrm{Mg} = 10$, $\mathrm{Eu} = 0$, $\delta = 2$, $\lambda = 2$, $\Lambda = 1$ and $\Delta_\chi = 1$, at the excitation wavenumber $k = 2$. The direction field associated with the fluid velocity $\mathbf{u}(x, y) = u(x, y)\mathbf{i} + v(x, y)\mathbf{j}$ is plotted at time instants t expressed as fractions of the period $T = 2\pi/|\Re(\omega)|$. The superimposed lines indicate the quiescent interface position (−−) and the corresponding harmonic disturbance (——) of arbitrary amplitude ($\epsilon = 0.1$). For illustrative purposes, the exponential temporal decay of the disturbance has been suppressed, so that $\Im(\omega)$ is artificially set to zero. Axis labels have been discarded for clarity, though the abscissa ranges over $0 \leqslant kx/\pi \leqslant 2$ and the ordinate ranges over $-1 \leqslant y \leqslant 1$ throughout (cf. Fig. 5).

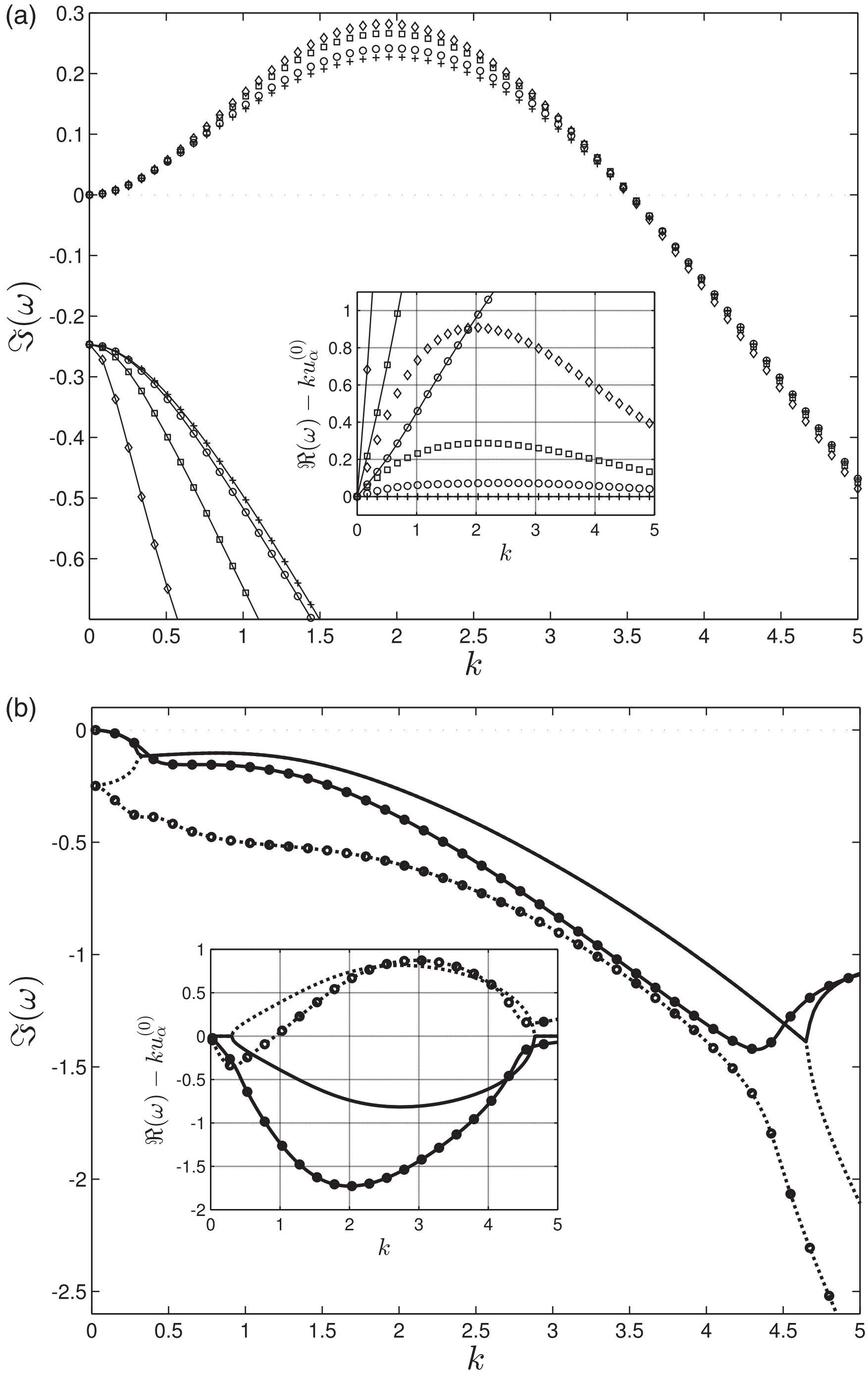

FIG. 9. Continued.

faster than the fluid $\Re(\omega)/k > u_\alpha^{(0)}$. Interestingly, we note that the second stable mode travels almost entirely without dispersion, at least over the wavenumber range $0 < k < 5$. For a more complicated situation involving mode interactions, Fig. 9(b) shows that the symmetry-breaking base state flow destroys the standing wave of the oscillatory state. The excited propagating waves are dispersive, and the dominant mode response is always more slowly moving than the base state flow at the interface.

7. Conclusions and further work

To investigate necessary conditions for the onset of turbulent mixing in a two-layer fluid system, this work considers the influence of a scalar concentration field on the linear stability of a fluid interface subject to small deformations under the regime of Stokes flow. The bulk concentration field is convected by the fluid flow and acts to non-uniformly alter the interfacial tension that, in turn, induces flow by the solutal Marangoni mechanism. This treatment of the solutal Marangoni effect is formally analogous to the thermocapillary effect, which arises when an interface is exposed to a spatially varying temperature field. In both scenarios, Marangoni tractions develop because of the local interfacial tension dependency on the strength of the ambient scalar field through a suitable constitutive relation. Zeren & Reynolds (1972) presented a linear stability analysis for the analogous thermocapillary problem, which also included the effect of buoyancy, but which assumed that the deformation of the interface was negligible. Interfacial deformation has been accounted for in more recent work by Tavener & Cliffe (2002) using a finite-element method. In this work, three distinct cases were studied, and we summarize these below.

In Case I, the solute diffusion is supposed to be instantaneous (crispation number $\mathrm{Cr} \to \infty$), but a finite Gibbs elasticity ($0 < \mathrm{Mg} < \infty$) permits interfacial displacements to generate a solutal Marangoni effect. Perturbations of the velocity and concentration fields are decoupled in this limit, so that the dispersion relation $\omega = \omega(k)$ between temporal response frequency ω and spatial excitation frequency k is obtained analytically. Furthermore, the stability behaviour is not sensitive to the mass diffusivity ratio Λ, effectively reducing the number of control parameters so that a complete stability diagram can be established. Only a single response mode is allowed where the interface is always stable to large k perturbations, but a region of unstable solutions exists at small wavenumber under certain conditions: that is a type II instability in the classification of Cross & Hohenberg (1993). The extent of these regions is found to be independent of the base-state flow field. For $\mathrm{Mg} > 0$, the interface is type II unstable when the viscosity ratio λ exceeds δ^2, where δ is the fluid film thickness ratio. Conversely, for $\mathrm{Mg} > 0$, unstable response is possible when $\lambda < \delta^2$. By determining the marginal stability bounds analytically, it is found that regions of global stability exist when $\mathrm{Mg} = 0$; or when $\mathrm{Mg} > 0$ and $\lambda < \delta^2$; or when $\mathrm{Mg} < 0$ and $1/\lambda < 1/\delta^2$.

FIG. 9. Temporal frequency dispersion curves $\omega = \omega(k)$ are shown for a fluid slab of uniform mass diffusivity ($\Lambda = 1$) and unit concentration difference on the bounding walls ($\Delta_\chi = 1$) at crispation number $\mathrm{Cr} = 0.1$. Panel (a): the growth rate $\Im(\omega)$ is compared between Case II ($\mathrm{Eu} = 0$)(+) and Case III with non-zero Eu set to 3(○), 10(□) and 30(◇), all obtained by the collocation method (Section 5.2). The dominant mode ($m = 1$) is indicated by symbols alone, whereas the secondary mode ($m = 2$) is denoted by symbols with solid lines. The inset shows the corresponding effective velocity $c_{\mathrm{rel}}/k = \Re(\omega) - ku_\alpha^{(0)}$ of the spatially propagating wave relative to the base state fluid speed on the interface. Other control parameters are $\lambda = 2$ and $\delta = 1/\sqrt{10} < \sqrt{\lambda}$ corresponding to an unstable response in Case I with $\mathrm{Mg} = 20$ (cf. Fig. 6(b)). Panel (b): a similar growth rate comparison between Case II ($\mathrm{Eu} = 0$) (no symbols) and Case III ($\mathrm{Eu} = 50$) (○) is shown. The dominant mode ($m = 1$) is indicated by solid lines (——), whereas the dotted line (· · ·) refers to the secondary mode ($m = 2$). Other control parameters are $\lambda = \delta = 2$ (corresponding to a stable response in Case I) with $\mathrm{Mg} = 100$ (cf. Fig. 7).

Case II permits comparable diffusion rates of matter and momentum but insists on zero Euler number ($\mathrm{Eu} = 0$), thereby removing the external pressure gradient and imposing a quiescent base state. Again, the dispersion relation is obtained, but the expression appears too cumbersome for analytic presentation of the stability diagram. In this case, our treatment is formally analogous to the classical linear stability analysis of the Rayleigh–Bérnard–Marangoni problem, but considers a realistic *deformable* interface leading to more complicated boundary conditions. As with the thermocapillary problem, an extremely rich discrete spectrum of modes is obtained, and several types of mode interaction are found. In particular, exceptional points exist between stationary and oscillatory standing wave solutions, but without the additional coupling between concentration and bulk mass density (that is, the solutal equivalent of the thermal buoyancy mechanism), there is no distinction between co-rotating and counter-rotating flow cells. Rather, the oscillatory state cycles between a counter-rotating pattern of four convection cells and a two-cell pattern. Furthermore, the merging of stationary states and their collapse into an avoided crossing of modes is seen as a function of control parameters, as well as evidence of resonant energy transfer and mode switching interactions between stationary and oscillatory states. Instabilities of both type II and type I in the Cross & Hohenberg (1993) classification are observed.

Case III is most general in that both Cr and Eu are unrestricted. A Chebyshev collocation method is implemented to solve the transport equations obeyed by the concentration perturbations. The presence of a background flow is potentially interesting because its impact on the overall system stability is not generally obvious. A surfactant-induced instability such as that found in the work of Frenkel & Halpern (2002), for instance, requires a base state shear component in order for unstable solutions to develop. In our analysis, a base-state flow was neither required for unstable solutions to exist nor were the regions of instability found to be extinguished by it. The evidence suggests that an external pressure gradient driving a base state flow generally exaggerates the response: by increasing the base flow speed, unstable growth rates are enhanced, and stable decay is suppressed. By breaking the isotropic symmetry of a quiescent base state, however, standing wave solutions are no longer possible for $\mathrm{Eu} > 0$.

At zero wavenumber, the general problem also yields to exact analysis where an infinite discrete spectrum of purely imaginary eigenvalues is determined and the response is proved to be always stable in this limit. Consequently, type III instabilities (Cross & Hohenberg, 1993) are precluded in this model. Furthermore, the mode spacing increases with crispation number so that only the single trivial zero frequency mode survives in the limit $\mathrm{Cr} \to \infty$, consistent with the Case I analysis.

Areas remaining open for further investigation include the following:

- the case of negligibly weak mass diffusion in both films where solute transport is entirely by fluid convection ($\mathrm{Cr} \to 0,\ 0 < \Lambda < \infty$) (intuition and evidence (e.g. Fig. 6(b)) suggests that instabilities are suppressed by boundary layers developing close to the interface—a matched asymptotic analysis is required to handle the change in order of the advection–diffusion equation in a non-regular limit);
- for the analogous Rayleigh–Bénard–Marangoni thermocapillary problem, the occurrence of Hopf bifurcations has been documented (Colinet & Legros, 1994) where time-dependent convection appears in a narrow transition region between stationary states. Can corresponding marginally stable bifurcation points be found in the present problem?
- in a departure from the thermocapillary analogue, the solutal Marangoni problem can consider the coupling of *many* scalar concentration fields, each with a distinct mass diffusivity in the bulk phases and a different contribution to the dilatational elasticity of the interface—can stability be modulated by tuning the adsorption of each solute type?

- what could be learned from an energy budget analysis to elucidate details of the instability mechanism (Boomkamp & Miesen, 1996; Albert & Charru, 2000; Yecko, 2008; Peng & Zhu, 2010)?
- what is the nature of the mechanism controlling the apparent transition between the appearance of two convection cells and four (see Fig. 5), and how does this phenomenon relate to interfacial stability? We speculate that the interface deformation and the proximity of bounding walls are involved as recently suggested by Pozrikidis & Hill (2011).

Ongoing research is applying this work to exploit the capability of the DGM as a physiologically relevant screening tool for evaluating novel and existing foodstuffs, diets and pharmaceutical preparations (Rickett, 2013). This will also inform the development of more realistic prototype machines.

Acknowledgement

This work was partially supported by the Biotechnology and Biological Sciences Research Council through its core strategic grant to the Institute of Food Research.

REFERENCES

ABRAMOWITZ, M. & STEGUN, I. A. (1965) *Handbook of Mathematical Functions*, 9th edn. New York: Dover Publications.

ALBERT, F. & CHARRU, F. (2000) Small Reynolds number instabilities in two-layer Couette flow. *Eur. J. Mech. B: Fluids*, **19**, 229–252.

ANDERECK, C. D., COLOVAS, P. W., DEGEN, M. M. & RENARDY, Y. Y. (1998) Instabilities in two layer Rayleigh–Bénard convection: overview and outlook. *Int. J. Eng. Sci.*, **36**, 1451–1470.

ANDERSON, D. M., MCFADDEN, G. B. & WHEELER, A. A. (1998) Diffuse-interface methods in fluids mechanics. *Annu. Rev. Fluid Mech.*, **30**, 139–165.

ANTURKAR, N. R., PAPANASTASIOU, T. C. & WILKES, J. O. (1990) Linear stability analysis of multilayer plane Poiseuille flow. *Phys. Fluids A*, **2**, 530–541.

BETCKE, T. & TREFETHEN, L. N. (2004) Computations of eigenvalue avoidance in planar domains. *Manchester Inst. Math. Sci., MIMS EPrint*, 2006.366.

BLYTH, M. G. & POZRIKIDIS, C. (2004a) Effect of surfactants on the stability of two-layer channel flow. *J. Fluid Mech.*, **505**, 59–86.

BLYTH, M. G. & POZRIKIDIS, C. (2004b) Effect of surfactant on the stability of film flow down an inclined plane *J. Fluid Mech.*, **521**, 241–250.

BLYTH, M. G. & POZRIKIDIS, C. (2004c) Effect of inertia on the Marangoni instability of two-layer channel flow, part II: normal-mode analysis. *J. Eng. Math.*, **50**, 329–341.

BODENSCHATZ, E., PESCH, W. & AHLERS, G. (2000) Recent developments in Rayleigh–Bénard convection. *Ann. Rev. Fluid Mech.*, **32**, 709–778.

BOOMKAMP, P. A. M. & MIESEN, R. H. M. (1996) Classification of instabilities in parallel two-phase flow. *Int. J. Multiphase Flow*, **22**, S67–S88.

BRAVERMAN, L. M., ECKERT, K., NEPOMNYASHCHY, A. A., SIMANOVSKII, I. B. & THESS, A. (2000) Convection in two-layer systems with an anomalous thermocapillary effect. *Phys. Rev. E*, **62**, 3619–3631.

CARTWRIGHT, J. H. E., GOUILLART, E., PIRO, N., PIRO, O. & TUVAL, I. (2012) Geometric mixing. http://arxiv.org/abs/1206.6894.

CHARRU, F. (2011) *Hydrodynamic Instabilities*. Cambridge: Cambridge University Press.

CHARRU, F. & HINCH, E. J. (2000) ‘Phase diagram’ of interfacial instabilities in a two-layer Couette flow and mechanism of the long-wave instability. *J. Fluid Mech.*, **414**, 195–223.

CHESSA, S., HUATAN, H., LEVINA, M., MEHTA, R. Y., FERRIZZI, D. & RAJABI-SIAHBOOMI, A. R. (2014) Application of the dynamic gastric model to evaluate the effect of food on the drug release characteristics of a hydrophilic matrix formulation. *Int. J. Pharm.*, **466**, 359–367.

COLINET, P. & LEGROS, J. C. (1994) On the Hopf bifurcation occurring in the two-layer Rayleigh–Bénard convective instability. *Phys. Fluids*, **6**, 2631–2639.

COWARD, A. V., RENARDY, Y. Y., RENARDY, M. & RICHARDS, J. R. (1997) Temporal evolution of periodic disturbances in two-layer Couette flow. *J. Comp. Phys.*, **132**, 346–361.

CRASTER, R. V. & MATAR, O. K. (2009) Dynamics and stability of thin liquid films. *Rev. Mod. Phys.*, **81**, 1131–1198.

CROSS, M. & GREENSIDE, H. (2009) *Pattern Formation and Dynamics in Nonequilibrium Systems*. Cambridge: Cambridge University Press.

CROSS, M. C. & HOHENBERG, P. C. (1993) Pattern formation outside of equilibrium. *Rev. Mod. Phys.*, **65**, 851–1112.

DRAZIN, P. G. (2002) *Introduction to Hydrodynamic Stability*. Cambridge: Cambridge University Press.

DRAZIN, P. G. & REID, W. H. (2004) *Hydrodynamic Stability*, 2nd edn. Cambridge: Cambridge University Press.

EDWARDS, D. A., BRENNER, H. & WASAN, D. T. (1991) *Interfacial Transport Processes and Rheology*. Boston: Butterworth-Heinemann.

FAN, J.-Y. (2003) A modified Levenberg–Marquardt algorithm for singular system of nonlinear equations. *J. Comp. Math.*, **21**, 625–636.

FRENKEL, A. L. & HALPERN, D. (2002) Stokes-flow instability due to interfacial surfactant. *Phys. Fluids*, **14**, L45–L48.

FRENKEL, A. L. & HALPERN, D. (2005) Effect of inertia on the insoluble-surfactant instability of a shear flow. *Phys. Rev. E*. *71,*, **016302**, 1–10.

GAO, P. & LU, X.-Y. (2007) Effect of surfactants on the inertialess instability of a two-layer film flow. *J. Fluid Mech.*, **591**, 495–507.

GOTTLEIB, D. & ORSZAG, S. A. (1977) *Numerical Analysis of Spectral Methods: Theory and Applications*. Bristol: SIAM.

HALPERN, D. & FRENKEL, A. L. (2003) Destabilization of a creeping flow by interfacial surfactant: linear theory extended to all wavenumbers. *J. Fluid Mech.*, **485**, 191–220.

HERNÁNDEZ, E., JÁUREGUI, A. & MONDRAGÓN, A. (2003) Unfolding a degeneracy point: crossings and anticrossings of unbound states in parameter space. *Rev. Mex. Fis.*, **49**, 60–72.

HINCH, E. J. (1984) A note on the mechanism of the instability at the interface between two shearing fluids. *J. Fluid Mech.*, **144**, 463–465.

HOOPER, A. P. (1985) Long-wave instability at the interface between two viscous fluids: thin layer effects. *Phys. Fluids*, **28**, 1613–1618.

HOOPER, A. P. & BOYD, W. G. C. (1983) Shear-flow instability at the interface between two viscous fluids. *J. Fluid Mech.*, **128**, 507–528.

JOHNSON, D. & NARAYANAN, R. (1997) Geometric effects on convective coupling and interfacial structures in bilayer convection. *Phys. Rev. E*, **56**, 5462–5472.

JOSEPH, D. D., BAI, R., CHEN, K. P. & RENARDY, Y. Y. (1997) Core-annular flows. *Annu. Rev. Fluid Mech.*, **29**, 65–90.

KATO, T. (1980) *Perturbation Theory for Linear Operators*, 2nd edn. Berlin: Springer.

KONG, F. & SINGH, R. P. (2008) Disintegration of solid foods in human stomach. *J. Food Sci.*, **73**, R67–R80.

KOSCHMIEDER, E. L. (1974) Bénard convection. *Adv. Chem. Phys.*, **26**, 177–212.

LAX, P. D. (2007) *Linear Algebra and its Applications*, 2nd edn. New York: Wiley and Sons.

LI, X. & POZRIKIDIS, C. (1997) The effect of surfactants on drop deformation and on the rheology of dilute emulsions in Stokes flow. *J. Fluid Mech.*, **341**, 165–194.

LI, J. & RENARDY, Y. (2000) Numerical study of flows of two immiscible liquids at low Reynolds number. *SIAM Review*, **42**, 417–439.

MARCIANI, L., FAULKS, R., WICKHAM, M. S. J., BUSH, D., PICK, B., WRIGHT, J., COX, E. F., FILLERY-TRAVIS, A. J., GOWLAND, P. A. & SPILLER, R. C. (2009) Effect of intragastric acid stability of fat emulsions on gastric emptying, plasma lipid profile and postprandial satiety. *Brit. J. Nutrition*, **101**, 919–928.

Marciani, L., Gowland, P. A., Spiller, R. C., Manoj, P., Moore, R. J., Young, P. & Fillery-Travis, A. J. (2001) Effect of meal viscosity and nutrients on satiety, intragastric dilution, and emptying assessed by MRI. *Am. J. Physiol. Gastrointest. Liver Physiol.*, **280**, G1227–G1233.

Marciani, L., Wickham, M. S. J., Bush, D., Faulks, R., Wright, J., Fillery-Travis, A. J., Spiller, R. C. & Gowland, P. A. (2006) Magnetic resonance imaging of the behaviour of oil-in-water emulsions in the gastric lumen of man. *Brit. J. Nutrition*, **95**, 331–339.

MATLAB (2013) *Version R2013a (8.1.0.604)*. Natick, Massachusetts: The Mathworks Inc.

Mercuri, A., Passalacqua, A., Wickham, M. S. J., Faulks, R. M., Craig, D. Q. M. & Barker, S. (2011) The effect of composition and gastric conditions on the self-emulsification process of ibuprofen-loaded self-emulsifying drug delivery systems: a microscopic and Dynamic Gastric Model study. *Pharm. Res.*, **28**, 1540–1551.

Merkt, D., Pototsky, A., Bestehorn, M. & Thiele, U. (2005) Long-wave theory of bounded two-layer films with a free liquid-liquid interface: Short- and long-time evolution. *Phys. Fluids*, **17**, 064104.

Nepomnyashchy, A., Simanovskii, I. & Legros, J. C. (2006) *Interfacial Convection in Multilayer Systems*. New York: Springer.

Normand, C., Pomeau, Y. & Velarde, M. G. (1977) Convective instability: a physicist's approach. *Rev. Mod. Phys.*, **49**, 581–624.

Oron, A., Davis, S. H. & Bankoff, S. G. (1997) Long-scale evolution of thin liquid films. *Rev. Mod. Phys.*, **69**, 931–980.

Pal, A., Brasseur, J. G. & Abrahamsson, B. (2007) A stomach road or 'Magenstrasse' for gastric emptying. *J. Biomech.*, **40**, 1202–1210.

Palmer, H. J. & Berg, J. C. (1972) Hydrodynamic stability of surfactant solutions heated from below. *J. Fluid Mech.*, **51**, 385–402.

Peng, J. & Zhu, K.-Q. (2010) Linear instability of two-fluid Taylor–Couette flow in the presence of surfactant. *J. Fluid Mech.*, **651**, 357–385.

Pozrikidis, C. (1997) Instability of two-layer creeping flow in a channel with parallel-sided walls. *J. Fluid Mech.*, **351**, 139–165.

Pozrikidis, C. (2004) Effect of inertia on the Marangoni instability of two-layer channel flow, part I: numerical simulations. *J. Eng. Math.*, **50**, 311–327.

Pozrikidis, C. & Hill, A. I. (2011) Surfactant-induced instability of a sheared liquid layer. *IMA J. Appl. Math.*, **76**, 859–875.

Rasenat, S., Busse, F. H. & Rehberg, I. (1989) A theoretical and experimental study of double-layer convection. *J. Fluid Mech.*, **199**, 519–540.

Reichenbach, J. & Linde, H. (1981) Linear perturbation analysis of surface-tension-driven convection at a plane interface (Marangoni instability). *J. Coll. Interface Sci.*, **84**, 433–443.

Renardy, Y. (1987a) The thin-layer effect and interfacial stability in a two-layer Couette flow with similar liquids. *Phys. Fluids*, **30**, 1627–1637.

Renardy, Y. (1987b) Viscosity and density stratification in vertical Poiseuille flow. *Phys. Fluids*, **30**, 1638–1648.

Rickett, L. (2013) A mathematical analysis of digestive processes in a model stomach. *Ph.D. Thesis*, University of East Anglia.

Sahu, K. C., Ding, H., Valluri, P. & Matar, O. K. (2009a) Linear stability analysis and numerical simulation of miscible two-layer channel flow. *Phys. Fluids*, **21**, 042104, 1–18.

Sahu, K. C., Ding, H., Valluri, P. & Matar, O. K. (2009b) Pressure-driven miscible two-fluid channel flow with density gradients. *Phys. Fluids*, **21**, 043603, 1–10.

Schmid, P. J. & Henningson, D. S. (2001) *Stability and Transition in Shear Flows*. New York: Springer.

Seyranian, A. P., Kirillov, O. N. & Mailybaev, A. A. (2005) Coupling of eigenvalues of complex matrices at diabolic and exceptional points. *J. Phys. A.: Math. Grn.*, **38**, 1723–1740.

Slavtchev, S., Hennenberg, M., Legros, J.-C. & Lebon, G. (1998) Stationary solutal Marangoni instability in a two-layer system. *J. Coll. Interface Sci.*, **203**, 354–368.

SLAVTCHEV, S., KALITZOVA-KURTEVA, P. & MENDES, M. A. (2006) Marangoni instability of liquid-liquid systems with a surface-active solute. *Coll. Surfaces A: Physiochem. Eng. Aspects*, **282–283**, 37–49.

SMITH, K. A. (1996) On convective instability induced by surface-tension gradients. *J. Fluid Mech.*, **24**, 401–414.

TALON, L. & MEIBURG, E. (2011) Plane Poiseuille flow of miscible layers with different viscosities: instabilities in the Stokes flow regime. *J. Fluid Mech.*, **686**, 484–506.

TAVENER, S. J. & CLIFFE, K. A. (2002) Two-fluid Marangoni-Bénard convection with a deformable interface. *J. Comp. Phys.*, **182**, 277–300.

THIFFEAULT, J.-L., GOUILLART, E. & DAUCHOT, O. (2011) Moving walls accelerate mixing. *Phys. Rev. E*, **84**, 036313–0.

WICKHAM, M. J. S., FAULKS, R. M., MANN, J. & MANDALARI, G. (2012) The design, operation, and application of a Dynamic Gastric Model. *Dissolution Tech.*, **19**, 15–22.

YECKO, P. (2008) Disturbance growth in two-fluid channel flow: the role of capillarity. *Int. J. Multiphase Flow*, **34**, 272–282.

YIH, C.-S. (1967) Instability due to viscosity stratification. *J. Fluid Mech.*, **27**, 337–352.

ZEREN, R. W. & REYNOLDS, W. C. (1972) Thermal instabilities in two-fluid horizontal layers. *J. Fluid Mech.*, **53**, 305–327.

ZHAO, A. X., WAGNER, C., NARAYANAN, R. & FRIEDRICH, R. (1995) Bilayer Rayleigh–Marangoni convection: transitions in flow structures at the interface. *Proc. Roy. Soc. Lond. A*, **451**, 487–502.

Appendix A

A.1 *General dispersion relation*

In the result (3.17) the coefficients are given by

$$
\begin{aligned}
\kappa_{\mathbf{u}} &= \kappa_{\mathbf{u}}^{(0)} + k_+^2((\alpha s_1 s_{1-\alpha} - k_- s_\alpha)\varOmega_{A2}(1) - (\alpha c_1 s_{1-\alpha} - k_- c_\alpha)\varOmega_{B2}(1) \\
&\quad - (s_1 s_{1-\alpha} - k_- s_\alpha)\varOmega_{C2}(1) + (c_1 s_{1-\alpha} - k_- c_\alpha)\varOmega_{D2}(1))\varLambda \\
&\quad - k_-^2((\alpha s_1 s_{1+\alpha} - k_+ s_\alpha)\varOmega_{A1}(-1) + (\alpha c_1 s_{1+\alpha} + k_+ c_\alpha)\varOmega_{B1}(-1) \\
&\quad - (s_1 s_{1+\alpha} + k_+ s_\alpha)\varOmega_{C1}(-1) - (c_1 s_{1+\alpha} - k_+ c_\alpha)\varOmega_{D1}(-1))\lambda, \\
\kappa_{\perp\boldsymbol{\sigma}} &= \kappa_{\perp\boldsymbol{\sigma}}^{(0)} + (s_{1+\alpha}^2 - k_+^2)((\alpha s_1 s_{1-\alpha} - k_- s_\alpha)\varOmega_{A2}(1) - (\alpha c_1 s_{1-\alpha} - k_- c_\alpha)\varOmega_{B2}(1) \\
&\quad - (s_1 s_{1-\alpha} - k_- s_\alpha)\varOmega_{C2}(1) + (c_1 s_{1-\alpha} - k_- c_\alpha)\varOmega_{D2}(1))\varLambda \\
&\quad - (s_{1-\alpha}^2 - k_-^2)((\alpha s_1 s_{1+\alpha} - k_+ s_\alpha)\varOmega_{A1}(-1) + (\alpha c_1 s_{1+\alpha} + k_+ c_\alpha)\varOmega_{B1}(-1) \\
&\quad - (s_1 s_{1+\alpha} + k_+ s_\alpha)\varOmega_{C1}(-1) - (c_1 s_{1+\alpha} - k_+ c_\alpha)\varOmega_{D1}(-1)), \\
\kappa_{\parallel\boldsymbol{\sigma}} &= k_-^2(s_{1+\alpha}^2 - k_+^2)\lambda - k_+^2(s_{1-\alpha}^2 - k_-^2), \qquad\qquad \text{(A.1)} \\
\kappa_\eta &= \kappa_\eta^{(0)} + 2(c_1 s_1 - k)((\alpha s_1 s_{1-\alpha} + k_- s_\alpha)\varOmega_{A1}(-1) - (c_1 s_{1-\alpha} + k_- c_\alpha)\varOmega_{D1}(-1) \\
&\quad - (\alpha s_1 s_{1+\alpha} + k_+ s_\alpha)\varLambda\varOmega_{A2}(1) - (c_1 s_{1+\alpha} + k_+ c_\alpha)\varLambda\varOmega_{D2}(1)) \\
&\quad + 2(c_1 s_1 + k)((\alpha c_1 s_{1-\alpha} + k_- c_\alpha)\varOmega_{B1}(-1) - (s_1 s_{1-\alpha} + k_- s_\alpha)\varOmega_{C1}(-1) \\
&\quad + (\alpha c_1 s_{1+\alpha} - k_+ c_\alpha)\varLambda\varOmega_{B2}(1) + (s_1 s_{1+\alpha} - k_+ s_\alpha)\varLambda\varOmega_{C2}(1)) \\
&\quad + (\lambda - 1)[2(c_1 s_1 - k)((\alpha s_1 s_{1-\alpha} + k_- s_\alpha)\varOmega_{A1}(-1) - (c_1 s_{1-\alpha} + k_- c_\alpha)\varOmega_{D1}(-1)) \\
&\quad + 2(c_1 s_1 + k)((\alpha c_1 s_{1-\alpha} + k_- c_\alpha)\varOmega_{B1}(-1) - (s_1 s_{1-\alpha} + k_- s_\alpha)\varOmega_{C1}(-1))
\end{aligned}
$$

$$
\begin{aligned}
&- (s_{1+\alpha}^2 - k_+^2)((\alpha s_1 c_{1-\alpha} + k_- c_\alpha)\mathit{\Omega}_{A2}(1) - (\alpha c_1 c_{1-\alpha} + k_- s_\alpha)\mathit{\Omega}_{B2}(1)\\
&- (s_1 c_{1-\alpha} + k_- c_\alpha)\mathit{\Omega}_{C2}(1) + (c_1 c_{1-\alpha} + k_- s_\alpha)\mathit{\Omega}_{D2}(1))\mathit{\Lambda}\\
&- (s_{1-\alpha}^2 - k_-^2)((\alpha s_1 c_{1+\alpha} - k_+ c_\alpha)\mathit{\Omega}_{A1}(-1) - (\alpha c_1 c_{1+\alpha} + k_+ s_\alpha)\mathit{\Omega}_{B1}(-1)\\
&- (s_1 c_{1+\alpha} + k_+ c_\alpha)\mathit{\Omega}_{C1}(-1) - (c_1 c_{1+\alpha} - k_+ s_\alpha)\mathit{\Omega}_{D1}(-1))],
\end{aligned}
$$

where the contributions independent of the chemical fields are

$$
\begin{aligned}
\kappa_{\mathbf{u}}^{(0)} &= -(k_+^2(c_{1-\alpha}s_{1-\alpha} - k_-) + k_-^2(c_{1+\alpha}s_{1+\alpha} - k_+))\lambda,\\
\kappa_{\perp\boldsymbol{\sigma}}^{(0)} &= -((s_{1+\alpha}^2 - k_+^2)(c_{1-\alpha}s_{1-\alpha} - k_-)\lambda + (s_{1-\alpha}^2 - k_-^2)(c_{1+\alpha}s_{1+\alpha} - k_+)),\\
\kappa_{\eta}^{(0)} &= \mathscr{A}_{k,\alpha}(\lambda - 1)^2 + 2\mathscr{B}_{k,\alpha}(\lambda - 1) + \mathscr{C}_k,\\
\mathscr{A}_{k,\alpha} &= (s_{1+\alpha}^2 - k_+^2)(c_{1-\alpha}^2 + k_-^2),\\
\mathscr{B}_{k,\alpha} &= \mathscr{A}_{k,\alpha} + (k_+k_-)^2 + \tfrac{1}{4}(s_{2(1+\alpha)}s_{2(1-\alpha)} - (2k_+)(2k_-)),\\
\mathscr{C}_k &= s_2^2 - (2k)^2.
\end{aligned}
\tag{A.2}
$$

Coupling terms between the flow and the chemical field involve the determinant-like functions

$$
\mathscr{L}_{k,\alpha}(\mathit{\Lambda}) = \det\begin{pmatrix} \det\begin{pmatrix} \mathit{\Psi}_1(-1) & \mathit{\Psi}_1(\alpha)\\ \mathit{\Phi}_1(-1) & \mathit{\Phi}_1(\alpha)\end{pmatrix} & \det\begin{pmatrix} \mathit{\Psi}_2(1) & \mathit{\Psi}_2(\alpha)\\ \mathit{\Phi}_2(1) & \mathit{\Phi}_2(\alpha)\end{pmatrix}\\ \mathscr{W}(\mathit{\Psi}_1(-1), \mathit{\Phi}_1(\alpha)) & \mathit{\Lambda}\mathscr{W}(\mathit{\Psi}_2(1), \mathit{\Phi}_2(\alpha))\end{pmatrix}, \tag{A.3}
$$

with $\mathscr{W}$ defined by (3.14) and

$$
\begin{aligned}
\mathit{\Omega}_{Xj}(y) = {}& \frac{k}{\mathit{\Psi}_j(y)\mathscr{L}_{k,\alpha}(\mathit{\Lambda})} \det\begin{pmatrix} \mathit{\Psi}_{3-j}(-y) & \mathit{\Psi}_{3-j}(\alpha)\\ \mathit{\Phi}_{3-j}(-y) & \mathit{\Phi}_{3-j}(\alpha)\end{pmatrix}\\
&\times \det\begin{pmatrix} \det\begin{pmatrix} \mathit{\Psi}_j(y) & \mathit{\Psi}_j(\alpha)\\ \mathscr{I}_{Xj}(y) & \mathscr{I}_{Xj}(\alpha)\end{pmatrix} & \det\begin{pmatrix} \mathit{\Psi}_j(y) & \mathit{\Psi}_j(\alpha)\\ \mathit{\Phi}_j(y) & \mathit{\Phi}_j(\alpha)\end{pmatrix}\\ \mathscr{W}(\mathit{\Psi}_j(y),\ \mathscr{I}_{Xj}(\alpha)) & \mathscr{W}(\mathit{\Psi}_j(y),\ \mathit{\Phi}_j(\alpha))\end{pmatrix}.
\end{aligned}
\tag{A.4}
$$

A.2 *Case II dispersion relation*

In the result (4.13) the coefficients are given by

$$
\begin{aligned}
\kappa_{\perp\boldsymbol{\sigma}}^{(1)} = \kappa_{\perp\boldsymbol{\sigma}}^{(0)} - \mathrm{Mg}\ \mathrm{Cr}\ & \frac{(1+\delta)\mathit{\Lambda}}{2(\delta + \mathit{\Lambda})} \frac{1}{\mathscr{L}_{k,\alpha}^{(1)}(\mathit{\Lambda})} \left(\frac{k}{\omega}\right)^2\\
&\times (S_{1,1+\alpha}(s_{1+\alpha}^2 - k_+^2)(K_2k_-(C_{2,1-\alpha} - c_{1-\alpha}) + (kS_{2,1-\alpha}s_{1-\alpha} - K_2(C_{2,1-\alpha}c_{1-\alpha} - 1))s_{1-\alpha})\mathit{\Lambda}\\
&- S_{2,1-\alpha}(s_{1-\alpha}^2 - k_-^2)(K_1k_+(C_{1,1+\alpha} - c_{1+\alpha}) + (kS_{1,1+\alpha}s_{1+\alpha} - K_1(C_{1,1+\alpha}c_{1+\alpha} - 1))s_{1+\alpha})),
\end{aligned}
$$

$$
\begin{aligned}
\kappa_\eta^{(1)} = \kappa_\eta^{(0)} &- \mathrm{Mg}\,\frac{(1+\delta)\Lambda}{4(\delta+\Lambda)}\,\frac{1}{\mathscr{L}_{k,\alpha}^{(1)}(\Lambda)}\left(\frac{1}{\omega}\right)\\
&\times ((K_1C_{1,1+\alpha}S_{2,1-\alpha} + K_2C_{2,1-\alpha}S_{1,1+\alpha})(k_+^2s_{1-\alpha}^2 - k_-^2s_{1+\alpha}^2)i\\
&+ (\lambda-1)(2kS_{1,1+\alpha}S_{2,1-\alpha}(k_+^2(c_{1-\alpha}s_{1-\alpha} + k_-) + k_-^2(c_{1+\alpha}s_{1+\alpha} + k_+))\\
&- (K_1C_{1,1+\alpha}S_{2,1-\alpha} + K_2C_{2,1-\alpha}S_{1,1+\alpha})k_-^2(s_{1+\alpha}^2 - k_+^2))i)\\
&- \mathrm{Mg}\,\mathrm{Cr}\,\frac{(1+\delta)\Lambda}{2(\delta+\Lambda)}\,\frac{1}{\mathscr{L}_{k,\alpha}^{(1)}(\Lambda)}\left(\frac{k}{\omega^2}\right)\\
&\times (2K_2S_{1,1+\alpha}((k(C_{2,1-\alpha}c_\alpha - c_1) + K_2S_{2,1-\alpha}s_\alpha)(c_1s_{1+\alpha} + k_+c_\alpha)(c_1s_1 - k)\\
&- (k(C_{2,1-\alpha}s_\alpha - s_1) + K_2S_{2,1-\alpha}c_\alpha)(s_1s_{1+\alpha} - k_+s_\alpha)(c_1s_1 + k))\Lambda\\
&- 2K_1S_{2,1-\alpha}((k(C_{1,1+\alpha}c_\alpha - c_1) - K_1S_{1,1+\alpha}s_\alpha)(c_1s_{1-\alpha} + k_-c_\alpha)(c_1s_1 - k)\\
&+ (k(C_{1,1+\alpha}s_\alpha + s_1) - K_1S_{1,1+\alpha}c_\alpha)(s_1s_{1-\alpha} + k_-s_\alpha)(c_1s_1 + k))\\
&+ (\lambda-1)(K_2S_{1,1+\alpha}(s_{1+\alpha}^2 - k_+^2)\\
&\times ((kC_{2,1-\alpha}c_{1-\alpha} - K_2S_{2,1-\alpha}s_{1-\alpha} - k)c_{1-\alpha} + k_-(ks_{1-\alpha} - K_2S_{2,1-\alpha}))\Lambda\\
&+ K_1S_{2,1-\alpha}(s_{1-\alpha}^2 - k_-^2)\\
&\times ((kC_{1,1+\alpha}c_{1+\alpha} - K_1S_{1,1+\alpha}s_{1+\alpha} - k)c_{1+\alpha} + k_+(ks_{1+\alpha} - K_1S_{1,1+\alpha})) + K_1S_{2,1-\alpha}\\
&\times (2k^2k_-(C_{1,1+\alpha} - c_{1+\alpha})k_+s_{1-\alpha} + (kC_{1,1+\alpha}c_{1-\alpha} + K_1S_{1,1+\alpha}s_{1-\alpha} - kc_2)k_+s_{1-\alpha}\\
&- (kC_{1,1+\alpha}c_{1+\alpha} - K_1S_{1,1+\alpha}s_{1+\alpha} - k)(s_2s_{1-\alpha} + k_-s_{1+\alpha})))). \qquad \text{(A.5)}
\end{aligned}
$$

A.3 *Proof* $\kappa_\eta^{(0)} > 0$

First note the obvious fact: if $a,\ b,\ c > 0$, then $a\lambda^2 + 2b\lambda + c > 0$ for all $\lambda > 0$. It follows that if $b > a > 0$ and $a - 2b + c > 0$, then

$$a\lambda^2 + 2(b-a)\lambda + a - 2b + c = a(\lambda-1)^2 + 2b(\lambda-1) + c > 0 \quad \text{for all } \lambda > 0. \qquad \text{(A.6)}$$

For the ‘jump’ term J_η, the coefficient $\kappa_\eta^{(0)}$ is a quadratic function of $(\lambda - 1)$, thus

$$\kappa_\eta^{(0)} = \mathscr{A}_{k,\alpha}(\lambda-1)^2 + 2\mathscr{B}_{k,\alpha}(\lambda-1) + \mathscr{C}_k, \qquad \text{(A.7)}$$

where

$$
\begin{aligned}
\mathscr{A}_{k,\alpha} &= (s_{1+\alpha}^2 - k_+^2)(c_{1-\alpha}^2 + k_-^2),\\
\mathscr{B}_{k,\alpha} &= \mathscr{A}_{k,\alpha} + (k_+k_-)^2 + \tfrac{1}{4}(s_{2(1+\alpha)}s_{2(1-\alpha)} - (2k_+)(2k_-)),\\
\mathscr{C}_k &= s_2^2 - (2k)^2.
\end{aligned} \qquad \text{(A.8)}
$$

By virtue of the fact that $\xi > 0$ implies $\sinh(\xi) > \xi$, we immediately observe

$$\mathscr{B}_{k,\alpha} > \mathscr{A}_{k,\alpha} > 0, \quad \mathscr{C}_k > 0, \qquad \text{(A.9)}$$

for all physically relevant parameter values. Furthermore, we find

$$\mathscr{A}_{k,\alpha}-2\mathscr{B}_{k,\alpha}+\mathscr{C}_k=(c_{1+\alpha}^2+k_+^2)(s_{1-\alpha}^2-k_-^2)>0. \tag{A.10}$$

So (A.7) satisfies the conditions for inequality (A.6). Hence, $\kappa_\eta^{(0)}>0$ for all $\lambda>0$, as claimed.

A.4 *Equivalence of (6.2) with (23) of Smith (1966)*

Recasting Smith's result (equation (23) of Smith (1966); see also equation (40) of Merkt *et al.* (2005) and equation (2.37) of Nepomnyashchy *et al.* (2006)) in our notation obtains

$$\begin{aligned}&-\frac{\mathrm{Mg}_0}{\mathrm{Cr}}\times\frac{4G_{\chi,1}}{(1+\delta)^2\varDelta_\chi}\left[1-\frac{1}{\varLambda}\left(\frac{g_{1+\alpha}s_{1+\alpha}(k_-^3c_{1-\alpha}-s_{1-\alpha}^3)}{g_{1-\alpha}s_{1-\alpha}(k_+^3c_{1+\alpha}-s_{1+\alpha}^3)}\right)\right.\\&\left.\quad-\frac{\mathrm{Cr}(1+\delta)^3}{(\mathrm{Bo}+k^2)}\left(\frac{k_+^3c_{1+\alpha}s_{1+\alpha}^2}{k_+^3c_{1+\alpha}-s_{1+\alpha}^3}\right)\left(1+\frac{c_{1-\alpha}s_{1+\alpha}}{c_{1+\alpha}s_{1-\alpha}}\right)\left(1-\lambda_0\frac{g_{1+\alpha}s_{1-\alpha}^2}{g_{1-\alpha}s_{1+\alpha}^2}-(1-\lambda_0)\frac{g_{1+\alpha}}{s_{1+\alpha}^2}\right)\right]\\&\quad=-4\left(\frac{k_+^2c_{1+\alpha}\mathscr{D}g_{1+\alpha}}{k_+^3c_{1+\alpha}-s_{1+\alpha}^3}\right)\left(1+\varLambda\frac{c_{1-\alpha}s_{1+\alpha}}{c_{1+\alpha}s_{1-\alpha}}\right)\left(1+\lambda_0\frac{g_{1+\alpha}\mathscr{D}g_{1-\alpha}}{g_{1-\alpha}\mathscr{D}g_{1+\alpha}}\right),\end{aligned} \tag{A.11}$$

where $\mathrm{Bo}=(\tilde{\rho}_1-\tilde{\rho}_2)\tilde{g}\tilde{h}^2/\tilde{\gamma}_0$ is the Bond number that measures the relative importance of capillary and gravitational forces (with acceleration $\tilde{g}$). By ignoring mass density stratification to set $\mathrm{Bo}=0$ and taking the limit $\mathrm{Cr}\to\infty$ in accord with our Case I, then (A.11) becomes

$$\begin{aligned}&\mathrm{Mg}_0\times\frac{4G_{\chi,1}k_+s_2}{(1+\delta)\varDelta_\chi}\left[s_{1+\alpha}^2-g_{1+\alpha}+\lambda_0g_{1+\alpha}\left(1-\frac{s_{1-\alpha}^2}{g_{1-\alpha}}\right)\right]\\&\quad=\mathrm{Mg}_0\times\frac{2\varLambda k_+s_2}{(\delta+\varLambda)}\left(k_+^2-\lambda_0k_-^2\frac{g_{1+\alpha}}{g_{1-\alpha}}\right)\\&\quad=-k_+^2\mathscr{D}g_{1+\alpha}(c_{1+\alpha}s_{1-\alpha}+\varLambda c_{1-\alpha}s_{1+\alpha})\left(1+\lambda_0\frac{g_{1+\alpha}\mathscr{D}g_{1-\alpha}}{g_{1-\alpha}\mathscr{D}g_{1+\alpha}}\right),\end{aligned} \tag{A.12}$$

or

$$\mathrm{Mg}_0=\frac{(\delta+\varLambda)(c_{1+\alpha}s_{1-\alpha}+\varLambda c_{1-\alpha}s_{1+\alpha})}{2\varLambda k_+s_2}\left(\frac{g_{1+\alpha}\mathscr{D}g_{1-\alpha}\lambda_0+g_{1-\alpha}\mathscr{D}g_{1+\alpha}}{g_{1+\alpha}\delta^2\lambda_0-g_{1-\alpha}}\right), \tag{A.13}$$

and using (4.8) recovers (6.2) as required.

A.5 *Proof in Case I* $\Re(\omega)\geqslant 0$

The argument follows the same structure as Section A.3. Recall that, in case $\mathrm{Cr}\to\infty$, the real part of the temporal frequency may be written proportional to a quadratic function in $(\lambda-1)$, thus

$$\Re(\omega)=\frac{\mathrm{Eu}}{\kappa_\eta^{(0)}(1+\delta)(\delta+\lambda)}(\mathscr{A}'_{k,\alpha}(\lambda-1)^2+2\mathscr{B}'_{k,\alpha}(\lambda-1)+\mathscr{C}'_k), \tag{A.14}$$

where

$$\begin{aligned} &\mathscr{A}'_{k,\alpha} = \mathscr{U}_{k,\alpha} + 2k\delta\mathscr{A}_{k,\alpha}, \quad \mathscr{B}'_{k,\alpha} = \tfrac{1}{2}(1-\delta^2)\mathscr{U}_{k,\alpha} + 2k\delta\mathscr{B}_{k,\alpha}, \quad \mathscr{C}'_k = 2k\delta\mathscr{C}_k, \\ \text{with}\quad &\mathscr{U}_{k,\alpha} = k_+^2(c_{1-\alpha}s_{1-\alpha} - k_-) + k_-^2(c_{1+\alpha}s_{1+\alpha} - k_+). \end{aligned} \tag{A.15}$$

Evidently, $\mathscr{U}_{k,\alpha} > 0$ and we find

$$\begin{aligned} k_+^2(\mathscr{B}'_{k,\alpha} - \mathscr{A}'_{k,\alpha}) &= k_+k_-(\mathscr{U}_{k,\alpha} + (k_+ + k_-)((k_+k_-)^2 + (c_{1-\alpha}s_{1-\alpha} - k_-)(c_{1+\alpha}s_{1+\alpha} - k_+))) \\ &\quad + (k_+k_-)^2(k_+ + k_-)(k_+ - k_-)^2 \sum_{n=0}^{\infty} \frac{2^{2n+1}}{(2n+1)!} \sum_{m=0}^{2n} k_+^{2n-m}k_-^m \\ &> 0, \end{aligned} \tag{A.16}$$

whence

$$\mathscr{B}'_{k,\alpha} > \mathscr{A}'_{k,\alpha} > 0. \tag{A.17}$$

Furthermore,

$$\mathscr{A}'_{k,\alpha} - 2\mathscr{B}'_{k,\alpha} + \mathscr{C}'_k = \delta^2\mathscr{U}_{k,\alpha} + 2k\delta(\mathscr{A}_{k,\alpha} - 2\mathscr{B}_{k,\alpha} + \mathscr{C}_k) > 0, \tag{A.18}$$

where the result of Section A.3 has been used. Hence, as claimed Eu > 0 implies $\Re(\omega) > 0$ for all $\lambda > 0$, while $\Re(\omega) = 0$ if Eu $= 0$.

A.6 *Proof* $k = 0$ *implies* $\Re(\omega) = 0$ *and* $\Im(\omega) \leqslant 0$

From the dispersion relation (5.18), we will deduce restrictions on the temporal frequency ω in the situation of vanishing wavenumber ($k = 0$). First recall the definitions (5.19):

$$\begin{aligned} &h_- = \frac{2\delta}{(1+\delta)\sqrt{\Lambda}} = \frac{1-\alpha}{\sqrt{\Lambda}} > 0; \quad h_+ = \frac{2}{1+\delta} = 1+\alpha > 0 \\ \text{and}\quad &K_0 = \sqrt{-i\omega/\mathrm{Cr}} = \Re(K_0) + i\,\Im(K_0) \in \mathbb{C} \end{aligned} \tag{A.19}$$

In particular,

$$\Re(K_0) = \sqrt{\frac{|\omega| + \Im(\omega)}{2\,\mathrm{Cr}}}, \tag{A.20}$$

so that

$$\begin{aligned} &\Re(K_0) = 0 \;\Rightarrow\; |\omega| + \Im(\omega) = 0 \\ \Rightarrow\; \Im(\omega) \leqslant 0 \quad \text{and} \quad &(\Im(\omega))^2 = (\Re(\omega))^2 + (\Im(\omega))^2 \;\Rightarrow\; \Re(\omega) = 0, \end{aligned} \tag{A.21}$$

since $|\omega| \geqslant 0$. Thus, it suffices to show that the dispersion relation (5.18) implies $\Re(K_0) = 0$.

For the sake of contradiction, suppose that $\Re(K_0) \neq 0$ while (5.18) holds. Now define

$$\hat{\mathscr{L}}^{(1)}_{0,\alpha} = \frac{\mathscr{L}^{(1)}_{0,\alpha}}{K_0 \cosh(\Re(K_0)h_-) \cosh(\Re(K_0)h_+)}, \tag{A.22}$$

so that

$$\begin{aligned} \Re(\hat{\mathscr{L}}^{(1)}_{0,\alpha}) &= T_-(c_-c_+ - s_-s_+\sqrt{\Lambda}) + T_+(c_-c_+\sqrt{\Lambda} - s_-s_+), \\ \Im(\hat{\mathscr{L}}^{(1)}_{0,\alpha}) &= T_-T_+(c_+s_-\sqrt{\Lambda} + c_-s_+) + (c_-s_+\sqrt{\Lambda} + c_+s_-), \end{aligned} \tag{A.23}$$

where

$$T_\pm = \tanh(\Re(K_0)h_\pm), \quad c_\pm = \cos(\Im(K_0)h_\pm), \quad s_\pm = \sin(\Im(K_0)h_\pm). \tag{A.24}$$

Since $\Re(K_0) \neq 0$ implies $T_-T_+ > 0$, then $\hat{\mathscr{L}}^{(1)}_{0,\alpha} = 0$ demands the bracketed factors in (A.23) either both vanish or are non-zero with opposite sign, so that

$$\begin{aligned} \Re(\hat{\mathscr{L}}^{(1)}_{0,\alpha}) = 0 \;&\Rightarrow\; (c_-c_+ - s_-s_+\sqrt{\Lambda})(c_-c_+\sqrt{\Lambda} - s_-s_+) \leqslant 0, \\ &\Rightarrow\; 0 \leqslant \frac{\sqrt{\Lambda}}{1+\Lambda}((c_-c_+)^2 + (s_-s_+)^2) \leqslant c_-s_-c_+s_+, \end{aligned} \tag{A.25}$$

$$\begin{aligned} \Im(\hat{\mathscr{L}}^{(1)}_{0,\alpha}) = 0 \;&\Rightarrow\; (c_+s_-\sqrt{\Lambda} + c_-s_+)(c_-s_+\sqrt{\Lambda} + c_+s_-) \leqslant 0, \\ &\Rightarrow\; c_-s_-c_+s_+ \leqslant -\frac{\sqrt{\Lambda}}{1+\Lambda}((c_-s_+)^2 + (c_+s_-)^2) \leqslant 0. \end{aligned} \tag{A.26}$$

Together, the conditions (A.25) and (A.26) require

$$c_-s_-c_+s_+ = 0. \tag{A.27}$$

Now consider the magnitude

$$\begin{aligned} |\hat{\mathscr{L}}^{(1)}_{0,\alpha}|^2 = {}& (c_-c_+)^2(T_- + T_+\sqrt{\Lambda})^2 + (c_-s_+)^2(T_-T_+ + \sqrt{\Lambda})^2 \\ &+ (c_+s_-)^2(T_-T_+\sqrt{\Lambda} + 1)^2 + (s_-s_+)^2(T_-\sqrt{\Lambda} + T_+)^2, \end{aligned} \tag{A.28}$$

where (A.27) has been used, and observe that $|\hat{\mathscr{L}}^{(1)}_{0,\alpha}| = 0$ requires

$$c_-c_+ = c_-s_+ = c_+s_- = s_-s_+ = 0, \tag{A.29}$$

again because $T_-T_+ > 0$. Finally, define

$$\Delta = \Im(K_0)(h_+ - h_-) \in \mathbb{R}, \tag{A.30}$$

and deduce that

$$\begin{aligned} c_-c_+ = s_-s_+ = 0 \;&\Rightarrow\; \cos\Delta = 0, \\ c_-s_+ = c_+s_- = 0 \;&\Rightarrow\; \sin\Delta = 0. \end{aligned} \tag{A.31}$$

But there is no real number Δ simultaneously satisfying both conditions (A.31). Hence, by contradiction, we conclude $\Re(K_0) = 0$, as required.